Scaling Description of Dynamical Heterogeneity and Avalanches of Relaxation in Glass-Forming Liquids

Ali Tahaei,[1] Giulio Biroli,[2] Misaki Ozawa,[3] Marko Popović,[1,4] and Matthieu Wyart[5]

[1]*Max Planck Institute for the Physics of Complex Systems, Nöthnitzer Strasse 38, 01187 Dresden, Germany*
[2]*Laboratoire de Physique de l'Ecole Normale Supérieure, ENS, Université PSL, CNRS, Sorbonne Université, Université Paris Cité, F-75005 Paris, France*
[3]*Université Grenoble Alpes, CNRS, LIPhy, 38000 Grenoble, France*
[4]*Center for Systems Biology Dresden, Pfotenhauerstrasse 108, 01307 Dresden, Germany*
[5]*Institute of Physics, EPFL, Lausanne, Switzerland*

(Received 4 May 2023; revised 21 July 2023; accepted 15 August 2023; published 21 September 2023)

We provide a theoretical description of dynamical heterogeneities in glass-forming liquids, based on the premise that relaxation occurs via local rearrangements coupled by elasticity. In our framework, the growth of the dynamical correlation length ξ and of the correlation volume χ_4 are controlled by a zero-temperature fixed point. We connect this critical behavior to the properties of the distribution of local energy barriers at zero temperature. Our description makes a direct connection between dynamical heterogeneities and avalanche-type relaxation associated to dynamic facilitation, allowing us to relate the size distribution of heterogeneities to their time evolution. Within an avalanche, a local region relaxes multiple times; the more, the larger the avalanche. This property, related to the nature of the zero-temperature fixed point, directly leads to decoupling of particle diffusion and relaxation time (the so-called Stokes-Einstein violation). Our most salient predictions are tested and confirmed by numerical simulations of scalar and tensorial thermal elastoplastic models. Our most salient predictions are tested and confirmed by numerical simulations of scalar and tensorial thermal elasto-plastic models, and in agreement with molecular dynamic simulations.

DOI: 10.1103/PhysRevX.13.031034 Subject Areas: Soft Matter, Statistical Physics

I. INTRODUCTION

As a liquid is cooled, the relaxation time τ_α below which it acts as a solid—before displaying flow—grows from picoseconds at high temperatures up to minutes at the glass transition temperature T_g [1–4]. In this regime, the effective activation energy associated to τ_α grows for many liquids, leading to a super-Arrhenius behavior. Approaching T_g, dynamics also becomes heterogeneous on a growing correlation length scale ξ [5–9]. The underlying causes for these observations are still debated. In some views, activation is cooperative: The slowing down of the dynamics is governed by complex motion taking place on an increasingly large static length scale. In particular, cooperativity is central in the random first-order theory [10–12] and due to the growth of amorphous order. Another approach focuses on dynamical facilitation, the phenomenon by which a region's relaxation is made much more likely by a relaxation nearby. In kinetically constrained models, such as the East model, kinetic rules induce dynamic facilitation and growth of dynamical correlations [13,14]. This lead to a theory [15–17] in which thermodynamics plays almost no role, but dynamics is heterogeneous (due to kinetic constraints) and the super-Arrhenius behavior is due to nonlocal rearrangements taking place over ξ. Free volume [18] or elastic [19–21] models assume that the activation energy is not controlled by a static growing length scale: It is governed by the energy barrier of elementary rearrangements or excitations. Recently, measurements indicated that the distribution of local energy barriers shifts to higher energy under cooling, opening up a gap at low energies where excitations are nearly absent [22]. This shift accounts quantitatively for the dynamical slowing down of the liquid, supporting that local energy barriers may indeed control the dynamics. Yet, in these views, what causes the existence of a growing length scale is unclear. An intuitive resolution of this paradox stems from the fact that, on relatively short timescales, a supercooled liquid acts as a solid [19,23]: A rearrangement corresponds to a local (plastic) strain, that affects stress away from it. Lemaitre [24] was the first in stressing the

possible relevance of long-range stress correlations in the dynamics of supercooled liquids, in line with various theoretical and numerical studies [25–31]. Recently, it was shown that indeed elastic interactions play an important role in dynamical facilitation [32]. Moreover, Ref. [33] showed that heterogeneous relaxations take place in the form of plastic rearrangements that are called shear transformations [34]. Following these molecular simulation studies, Ref. [35] demonstrated with elastoplastic models (traditionally used to study the plasticity of amorphous solids under loading [36–40]) that, while being controlled by local energy barriers, the dynamics can at the same time display growing dynamical correlations similar to observations in experiments and molecular simulations [14,41]. Furthermore, such models also capture the emergence of a gap in the distribution of local barriers under cooling, which controls the dynamics [35,42]. We expect that the elastoplastic description discussed above becomes more and more relevant with decreasing temperature. This paper focuses on such a lower-temperature regime.

In this work, we propose a scaling description of dynamical heterogeneities in glass-forming liquids, modeled as undergoing local irreversible rearrangements coupled by elasticity. We show that the dynamical correlations observed in elastoplastic models of equilibrium glassy dynamics [35] are due to "thermal avalanches," where rare nucleated events are followed by a pulse of faster (or facilitated) events. These avalanches are very reminiscent of the ones found in molecular simulations of supercooled liquids [43–45]. Our analysis builds a link with systems that crackle such as disordered magnets, granular materials, and earthquakes [46,47] even at finite temperatures [42,48–50], revealing that dynamical heterogeneities are controlled by a critical point at zero temperature, with a diverging length scale $\xi \sim T^{-\nu}$ and correlation volume $\chi_4^* \sim T^{-\gamma}$. We provide a scaling argument expressing ν and γ in terms of the distribution of energy barriers at $T = 0$. Our analysis makes predictions on the power-law distribution of the size of dynamical heterogeneities, which could be tested in numerical simulations of supercooled liquids thanks to the recent advances in the characterization of dynamical correlations [51,52]. Based on the properties of the zero-temperature fixed point governing thermal avalanches, we also show that the decoupling $D\tau_\alpha$ between particle diffusion D and relaxation time τ_α (the so-called Stoke-Einstein violation [53–57]) diverges as $D\tau_\alpha \sim T^{-h}$, where h can be expressed in terms of avalanche properties at vanishing temperature. The key physical mechanism behind the Stoke-Einstein violation is the intensive accumulation of rearrangements in the mobile region that quantifies a larger diffusion constant D, relative to the structural relaxation time τ_α [58–62]. We perform numerical simulations and analyze the results by finite-size scaling in order to test our salient predictions. Our findings agree well with the scaling theory for both scalar and tensorial thermal elastoplastic models.

II. THERMAL ELASTOPLASTIC MODELS

To study dynamical heterogeneities in low-temperature glass-forming liquids, we employ a generalization of elastoplastic models [36,37] which are a class of mesoscopic models designed to capture the essential features of localized plastic events (shear transformations) with stress relaxation accompanied by long-range elastic interactions. An elastoplastic model contains $N = L^d$ mesoscopic sites that are arranged on a regular grid whose linear size is L, and d is the spatial dimension. Each site exhibits a plastic event when the magnitude of the local shear stress becomes sufficiently large, which leads to local stress relaxation and stress redistribution in the rest of the system via the form of Eshelby fields. Elastoplastic models were originally introduced to study the flow of amorphous solids under external loading [36,37,39,40] (some exceptions, e.g., Ref. [63]), and they were generalized to take into account thermal fluctuations [64] and then to study glass-forming liquids [35]. Here, we study their low-temperature relaxation dynamics in the absence of loading. Following the idea that supercooled liquids can be viewed as solids that flow [19,24], we develop a physical scenario based on the assumption that local rearrangements are elastically coupled, and we model this physical mechanism by elastoplastic models.

In this paper, we use a tensorial elastoplastic model that accounts for the shear stress tensor [65] and a scalar elastoplastic model in which the shear stress is represented by a scalar variable [35] (see Appendix A for details). In both models, thermal fluctuations are implemented through a probability rate $\tau_0^{-1} e^{-E/T}$ to trigger a plastic (mobile) event in an otherwise stable elastic (immobile) site, where E is the local activation energy barrier and τ_0 is a microscopic relaxation timescale [42,64,66,67]. The energy barrier E can be related to the minimal amount of additional shear stress x_i required to destabilize a site i. In particular, we consider $E(x) = cx^\alpha$, which is suggested by recent elastoplastic models and molecular simulations [33,42,66–68]. In this study, we set $\tau_0 = 1$, $c = 1$, and the value $\alpha = 3/2$ corresponds to a smooth microscopic potential [69]. As stress is relaxed locally at the site of the plastic event, stress in the system changes according to the Eshelby kernel [36]. Specifically, in the scalar model, the kernel is randomly oriented at each relaxation event. This random orientation of the Eshelby kernel is crucial to describe for isotropic supercooled liquids in a quiescent state, in contrast to amorphous solids under shear, where Eshelby fields align along the shear direction [70]. Note that, in the tensorial model, after each relaxation the yielding surface is reoriented uniformly at random, and one uses the full Eshelby propagator; hence, no additional symmetrization is required [71]. Besides, our elastoplastic models have zero total (macroscopic) stress, as anticipated

in quiescent supercooled liquids. Detailed descriptions of the tensorial and scalar models are found in Appendix A. We perform numerical simulations in a two-dimensional periodic lattice ($d = 2$), whereas we develop scaling arguments in general d dimensions. Since we find that both scalar and tensor models show qualitatively and quantitatively similar results (e.g., critical exponents), we focus on the tensorial model in the main text and present the scalar one in Appendixes B and C.

III. DYNAMICAL HETEROGENEITIES AT FINITE TEMPERATURES

We first perform finite-temperature simulations and characterize dynamical properties. To this end, we consider the persistence two-point time correlation function $\langle \pi(t) \rangle_{\rm time}$, which is used widely in the context of kinetically constrained models [13]. The observable $\pi(t)$ is defined by $\pi(t) = \sum_i p_i(t)/N$, where $p_i(t) = 1$ if the site i does not exhibit a plastic event until time t and remains immobile and $p_i(t) = 0$ for mobile sites that relax at least once. The notation $\langle \cdots \rangle_{\rm time}$ denotes the time average at the stationary state at temperature T reached after a long enough equilibration time. We verify that the model does show dynamical slowing down by measuring $\langle \pi(t) \rangle_{\rm time}$ at different temperatures, as shown in Fig. 1(a). In Fig. 1(b), we find that the associated relaxation time τ_α defined by $\langle \pi(\tau_\alpha) \rangle_{\rm time} = 1/2$ increases in an Arrhenius way. Figure 2(a) represents a snapshot of local persistence for $\tau/\tau_\alpha \simeq 0.53$, demonstrating spatially heterogeneous dynamics. To quantify the magnitude of dynamical heterogeneity, we compute the four-point correlations function [72] $\chi_4(t)$, defined by

$$\chi_4(t) = N(\langle \pi^2(t) \rangle_{\rm time} - \langle \pi(t) \rangle^2_{\rm time}). \tag{1}$$

$\chi_4(t)$ is proportional to the size of the dynamically correlated region (see Appendix B for details), which is the central observable characterizing dynamical heterogeneity approaching the glass transition [14], as it has been

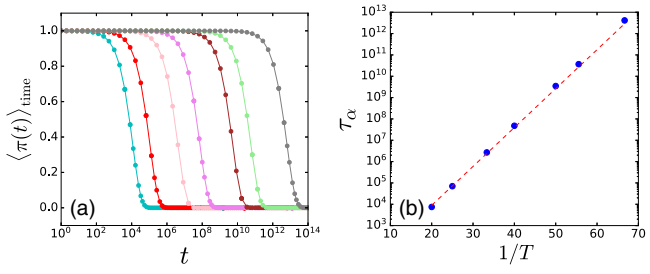

FIG. 1. Dynamics of the tensorial model in finite-temperature simulations. (a) Mean persistence correlation function $\langle \pi(t) \rangle_{\rm time}$ for $L = 128$ and $T = 0.050$, 0.040, 0.030, 0.025, 0.020, 0.018, and 0.015 (from left to right). (b) The relaxation time τ_α versus $1/T$. The red dashed line corresponds to $\tau_\alpha \sim e^{E_c/T}$ with $E_c = x_c^{3/2} = 0.42$ measured independently in Sec. IV.

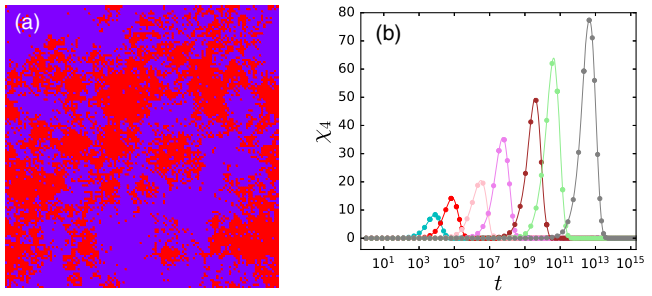

FIG. 2. Dynamical heterogeneity of the tensorial model in finite-temperature simulations. (a) Snapshot characterized by local persistence $p_i(\tau)$ when $\tau/\tau_\alpha \approx 0.53$ at $T = 0.015$. Red and purple sites correspond to mobile [$p_i(\tau) = 0$] and immobile [$p_i(\tau) = 1$] sites, respectively. The system size is $L = 128$. (b) Four-point correlation function $\chi_4(t)$ for $L = 128$ and $T = 0.050$, 0.040, 0.030, 0.025, 0.020, 0.018, and 0.015 (from left to right).

estimated in real experiments [7,41,73,74] as well as molecular simulations [72,75,76].

Figure 2(b) shows the time and temperature evolution of $\chi_4(t)$. It takes a peak near the relaxation timescale τ_α, and the peak grows with decreasing temperature, which is the hallmark of dynamical heterogeneity in glassy dynamics. We then plot the peak value of $\chi_4(t)$, denoted χ_4^*, versus temperature T for several system sizes in Fig. 3(a). The system size dependence, akin to molecular simulations [75,77], allows us to perform finite-size scaling. We find that, for increasing the system size L, χ_4^* follows a scaling form $\chi_4^* \sim T^{-\gamma}$ with a critical point at $T = 0$ and the associated exponent γ. We obtain a scaling collapse for $\chi_4^*(L, T)$ in Fig. 3(b) (see also molecular simulation studies [75,77]), indicating that the dynamics is governed by a diverging correlation length toward $T = 0$, i.e., $\xi \sim T^{-\nu}$ with an exponent ν. The corresponding data for the scalar model are presented in Appendix B. Besides, we obtain a consistent result in terms of ν by directly measuring the dynamical correlation length scale based on the four-point structure factor [78]. The observed critical exponents and predictions (see below) are summarized in Table I. The main goal of this paper is to provide a scaling theory for these critical behaviors, connecting the dynamics at finite temperature to a zero-temperature critical point.

IV. CRITICAL POINT AND EXTREMAL DYNAMICS AT $T = 0^+$

We now consider dynamics at vanishing temperature $T = 0^+$ and show that it is related to a critical point. At $T = 0^+$, the site with the smallest energy barrier $E_{\rm min} = x_{\rm min}^{3/2}$, the weakest site, always yields first [79], where $x_{\rm min}$ is the corresponding stress required to destabilize the site. Therefore, one can simulate dynamics at $T = 0^+$ by relaxing always the weakest site instead of relaxing a random site weighted by the relaxation rate

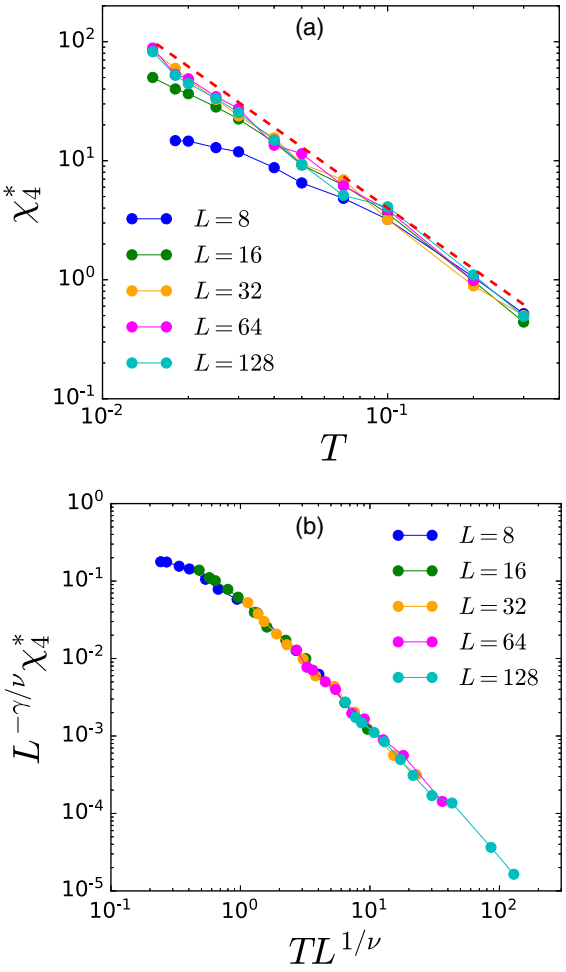

FIG. 3. (a) The peak of four-point correlation function χ_4^* versus T for several L for the tensorial model. The red dashed line follows $\chi_4^* \sim T^{-\gamma}$. (b) The corresponding scaling collapse.

$e^{-E(x)/T}$. This algorithm allows us to access dynamical information even at vanishing temperature (see details in Appendix C). It is an example of *extremal dynamics*, which is well studied in the context of self-organized criticality [80] and some disordered materials under quasistatic driving [48,81], including annealed glasses [82].

In the thermodynamic limit $L \to \infty$, the extremal dynamics leads to an absorbing condition for $E \leq E_c$, where E_c is a critical energy barrier as found (for $T \to 0$) in Ref. [35]. As a result, the distribution of local (activation) energy barriers $P(E)$ vanishes for $E \leq E_c$ [see the sketch in Fig. 8(a)]. This implies that $\lim_{L\to\infty} P(x) = 0$ for $x \leq x_c = E_c^{2/3}$, where $P(x)$ is the distribution of x. Thus, only a subextensive number of sites are found for $x \leq x_c$ at a finite L. In this paper, we use $P(E)$ and $P(x)$ interchangeably, since they carry essentially the same information.

The extremal dynamics consists of a succession of avalanches. In fact, relaxation at a site can change local energy barriers E at different sites by elastic interactions. As long as those are below E_c, the corresponding sites belong to the same avalanche [80]. This is a vivid realization of the phenomenon of dynamic facilitation. To characterize the avalanches, we follow the method introduced in the study of extremal dynamics [48,80]. For a finite L, we fix a chosen threshold stability value $x_0 (\leq x_c)$ and define x_0 *avalanches* as the sequences of events for which $x_{\min} < x_0$ (see Fig. 16 in Appendix C). Two useful characterizations of avalanche size are the total number of relaxation events S in a given sequence (event-based avalanche size) and the total number of sites $\tilde{S}$ that relaxed at least once during an avalanche (site-based avalanche size). By construction, $\tilde{S} \leq S$ and $\tilde{S} \leq L^d$. We show a snapshot having S and the corresponding $\tilde{S}$ in Fig. 4. The two characterizations can be (and, as we show, are) different, as a site can relax multiple times within the same avalanche. Thus, the event-based avalanche size S allows us to quantify the accumulation of relaxation events in the mobile region (as emphasized in a recent molecular

TABLE I. Critical exponents (γ and ν) obtained from finite T simulations in the scalar and tensorial elastoplastic models in two dimensions, compared with their predicted values proposed in Sec. V.

	Scalar model	Tensorial model	Prediction $d=2$	Prediction mean-field
γ	1.8 ± 0.1	1.7 ± 0.1	1.60 ± 0.05	1.5
ν	0.85 ± 0.05	0.80 ± 0.05	0.80 ± 0.03	0.75

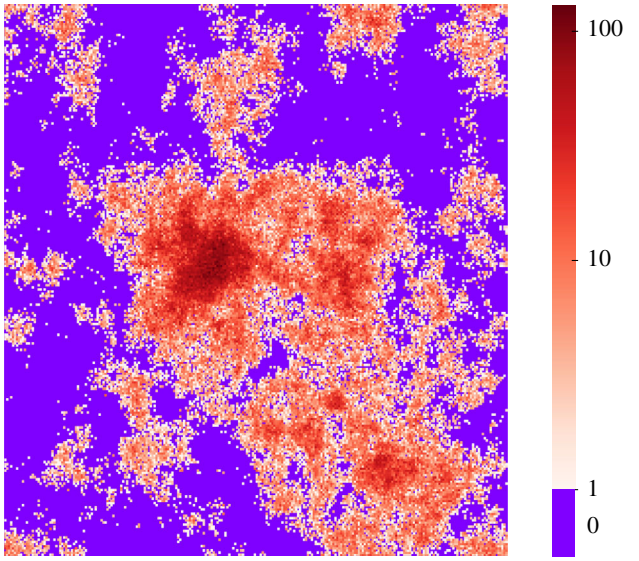

FIG. 4. A snapshot of an avalanche formation for the extremal dynamics of the tensorial model with $L = 256$. Event-based avalanche size is $S \simeq 2.7 \times 10^5$, while the site-based avalanche size is $\tilde{S} \simeq 3 \times 10^4$. Purple shows immobile sites (zero event), and the color bar shows the number of relaxation events in mobile sites.

simulation study [52]), whereas the site-based avalanche size $\tilde{S}$ is associated to the spatial extent of dynamically correlated regions [as it contains the essentially same information as the persistence map in Fig. 2(a) and, hence, χ_4]. Sizes of avalanches, S and $\tilde{S}$, depend on the threshold x_0. They grow with increasing x_0 and diverge at x_c.

By systematically exploring different values of x_0, one can determine the critical point x_c. In fact, one expects that the avalanche distribution $P(S)$ during the extremal dynamics follows a power law with a scaling form [48,80,83]:

$$P(S) \sim S^{-\tau} g(S/S_c), \tag{2}$$

where $g(z)$ is a scaling function and S_c is a cutoff size which takes the form

$$S_c \sim (x_c - x_0)^{-1/\sigma} f\left(\frac{L^{d_f}}{(x_c - x_0)^{-1/\sigma}}\right), \tag{3}$$

where $1/\sigma$ and d_f are critical exponents, $f(z) = 1$ for $z \gg 1$, and $f(z) = z$ for $z \to 0$. Thus, $S_c \sim L^{d_f}$ when $x_0 \to x_c$, whereas $S_c \sim (x_c - x_0)^{-1/\sigma}$ when $L \to \infty$. The same expressions are expected to hold for the site-based avalanche size $\tilde{S}$, defining exponents $\tilde{\tau}$, $1/\tilde{\sigma}$, and $\tilde{d}_f$. To estimate S_c, we use the fact that for $1 < \tau < 3$ the ratio $\langle S^3 \rangle / \langle S^2 \rangle$ is proportional to the cutoff value S_c, where $\langle \cdots \rangle = \int_0^\infty dS P(S)(\cdots)$. As we are interested in scaling of S_c with system size, the numerical constant is irrelevant and we define $S_c \equiv \langle S^3 \rangle / \langle S^2 \rangle$. The same expression is used *mutatis mutandis* for the site-based avalanche size $\tilde{S}$. More details about avalanche statistics can be found in Appendix C.

We determine x_c and the exponents $1/\sigma$, $1/\tilde{\sigma}$, d_f, and $\tilde{d}_f$ by measuring S_c and $\tilde{S}_c$ for different values of threshold x_0 and system size L and collapsing them using the scaling form in Eq. (3) for both S_c and $\tilde{S}_c$, as shown in Figs. 5(a) and 5(b). We obtain $x_c = 0.560 \pm 0.001$. The values of the critical exponents are presented in Table II. Figures 5(c) and 5(d) display S_c and $\tilde{S}_c$ as a function of $x_c - x_0$, for various system sizes L. They indeed show that S_c and $\tilde{S}_c$ grow with x_0 and saturate due to finite-size effects.

Once x_c is determined, we can study the statistics of the system-spanning avalanches relevant to the thermodynamic limit. Thus, we fix $x_0 = x_c$ and measure the distribution $P(S)$ and $P(\tilde{S})$ of the avalanche sizes; see Figs. 6(a) and 6(b). We find that avalanche sizes are power-law distributed with an eventual cutoff, consistent with the general assumption in Eq. (2). The scaling form in Eq. (2) collapses the data using $S_c \sim L^{d_f}$ and the previously obtained values of d_f and $\tilde{d}_f$; see Figs. 6(c) and 6(d). From the data collapse, we determine values of avalanche exponents τ and $\tilde{\tau}$ (see Table II). The successful collapse of the data confirms the validity of the scaling ansatz as well as the value of critical exponents.

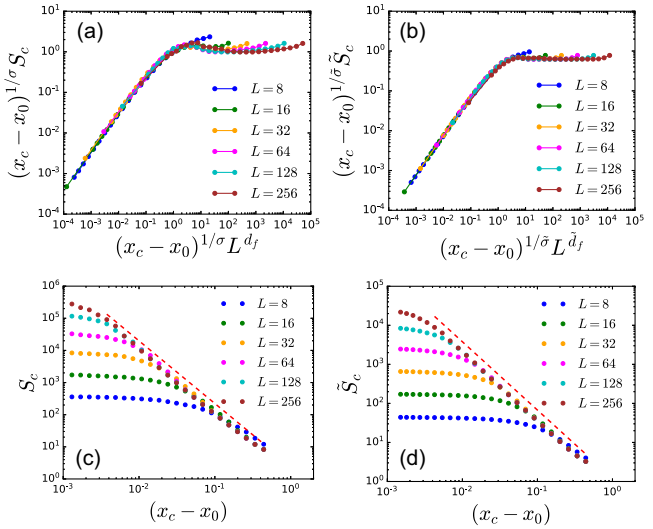

FIG. 5. Statistical properties of avalanches during the extremal dynamics at $T = 0^+$ for the tensorial model. (a),(b) Scaling collapse for the cutoff size $S_c = \langle S^3 \rangle / \langle S^2 \rangle$ based on Eq. (3), for various L for the event-based (a) and site-based (b) avalanche sizes, which determines the critical threshold x_c and critical exponents $1/\sigma$, $1/\tilde{\sigma}$, d_f, and $\tilde{d}_f$. (c),(d) S_c versus $x_c - x_0$. The red dashed line corresponds to $S_c \sim (x_c - x_0)^{-1/\sigma}$ in (c) and $\tilde{S}_c \sim (x_c - x_0)^{-1/\tilde{\sigma}}$ in (d).

The above analysis reveals that the extremal dynamics of our model of glass forming-liquid displays, scale-free, avalanche-type dynamics akin to the ones of other disordered systems under external loading [46,47].

Coming back to the distribution of energy barriers $P(E)$ and the corresponding distribution $P(x)$, one would expect that it continuously vanishes at x_c as $P(x) \sim (x - x_c)^\theta$, defining an exponent θ [42]. This behavior also occurs near the yielding transition of amorphous solids under shearing (with $x_c = 0$) [84], where it affects the scaling of flow properties [39] and plasticity [85], and, more generally, in glassy systems with long-range interactions [86].

TABLE II. Critical exponents obtained from extremal dynamics simulations at $T = 0^+$ for the scalar and tensorial elastoplastic models in two dimensions. The reported error for the measured exponents corresponds to the range of parameters over which the power-law behavior successfully collapses the data.

Scalar model	Tensorial model
$\delta = 0.64 \pm 0.01$	$\delta = 0.62 \pm 0.01$
$\tau = 1.25 \pm 0.05$	$\tau = 1.30 \pm 0.05$
$d_f = 2.3 \pm 0.1$	$d_f = 2.3 \pm 0.1$
$1/\sigma = 2.2 \pm 0.1$	$1/\sigma = 1.95 \pm 0.03$
$\tilde{\tau} = 1.25 \pm 0.05$	$\tilde{\tau} = 1.35 \pm 0.03$
$\tilde{d}_f = 2.00 \pm 0.02$	$\tilde{d}_f = 1.95 \pm 0.05$
$1/\tilde{\sigma} = 1.9 \pm 0.1$	$1/\tilde{\sigma} = 1.75 \pm 0.03$

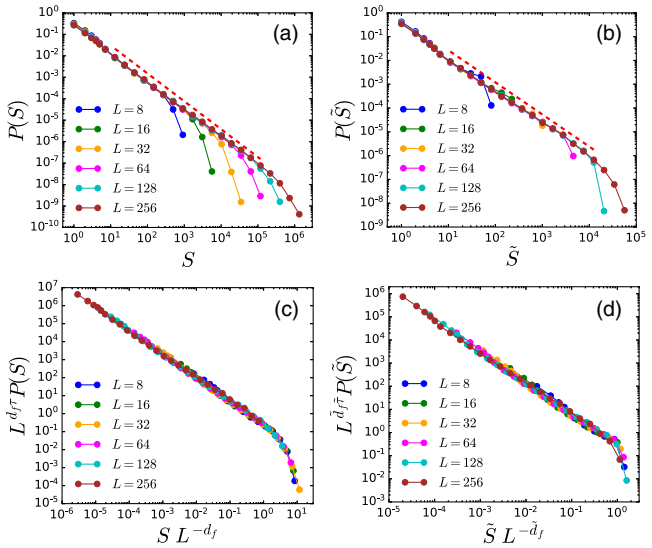

FIG. 6. (a),(b) Distribution of avalanche size $P(S)$ (a) and $P(\tilde{S})$ (b) for a stability threshold $x_0 = x_c$ for the tensorial model, with varying the system size L. The dashed lines follow $P(S) \sim S^{-\tau}$ (a) and $P(\tilde{S}) \sim \tilde{S}^{-\tilde{\tau}}$ (b). (c),(d) The corresponding scaling collapse following Eq. (2) with $S_c \sim L^{d_f}$ (c). The same expressions are used for $P(\tilde{S})$ in (d).

The underlying reason is that, at each step of the extremal dynamics, each site receives a stress kick, such that x_i of a site i follows a random process, with an effective absorbing condition at x_c. If this random process were a Brownian motion, then one would obtain $\theta = 1$. Yet the kicks are much more broadly distributed, and, in higher dimensions, this random process is akin to a Levy flight [87], which can be shown to imply $\theta_{\mathrm{MF}} = 1/2$ [88]. In Fig. 7(a), we plot $P(x)$ for the extremal dynamics, measured from configurations just before (or after) each avalanche defined as $x_{\min} > x_0 = x_c$, together with $P(x)$ obtained from finite-temperature simulations studied in Sec. III. At higher T, $P(x)$ shows a broader distribution with a smooth decay. As T is decreased, $P(x)$ converges to the one obtained by the extremal dynamics at $T = 0^+$, whose shape is consistent with $P(x) \sim (x - x_c)^{\theta}$.

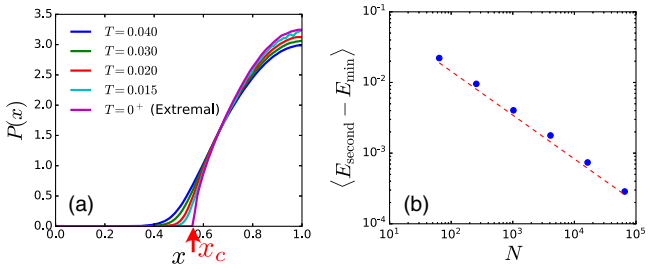

FIG. 7. (a) $P(x)$ from finite T simulations and extremal dynamics at $T = 0^+$ for the tensorial model with $L = 256$. The red arrow indicates x_c. (b) Average of $E_{\mathrm{second}} - E_{\mathrm{min}}$ obtained from the extremal dynamics for various $N = L^d$. The red dashed line corresponds to $\langle E_{\mathrm{second}} - E_{\mathrm{min}} \rangle \sim N^{-\delta}$.

The following two features of $P(x)$ connect the extremal and finite-temperature dynamics. First, the point x_c or the corresponding energy scale $E_c = x_c^{3/2}$ controls the effective energy barrier associated to τ_α. Indeed, at small temperature, the dynamics proceeds by relaxing the sites with smallest barriers, i.e., sites having barriers close to E_c [35,42]. This is in agreement with the relaxation time τ_α observed in Fig. 1(b), which scales as $\tau_\alpha \sim e^{E_c/T}$.

Second, more importantly for what follows, in a finite system of size $N = L^d$, the typical scale of $x_{\min}$ and the second-lowest x, denoted as x_{second}, is expected to follow a power law, $\langle x_{\mathrm{second}} - x_{\min} \rangle \sim N^{-\delta}$. As we show, this plays a key role in the characterization of thermal avalanches. Since the energy difference between the lowest and second-lowest activation energies is given by $E_{\mathrm{second}} - E_{\min} \sim x_{\mathrm{second}} - x_{\min}$, we conclude

$$\langle E_{\mathrm{second}} - E_{\min} \rangle \sim N^{-\delta}. \tag{4}$$

Thus, the exponent δ characterizes an important feature of the energy barrier relevant for low-temperature dynamics. We numerically confirm this scaling in Fig. 7(b), and the obtained value of δ is reported in Table II. Extreme value statistics argument suggest $\delta = 1/(1+\theta)$ [39] (although near the yielding point deviations from this relation have been reported in finite dimension [89] and explained in Ref. [90]). Within the mean-field theory [88], one finds $\delta_{\mathrm{MF}} = 1/(1+\theta_{\mathrm{MF}}) = 2/3$, a value close to what we observe in Fig. 7(b).

The results presented in this section show that the extremal dynamics of the tensorial elastoplastic model of supercooled liquids is governed by system-spanning avalanches. We fully characterize the associated zero-temperature critical point by obtaining all relevant exponents, summarized in Table II. We also obtain qualitatively and quantitatively (e.g., critical exponents) similar results in the scalar model, which are presented in Appendix C. Remarkably, we find that the scalar and tensorial models display very close values of the critical exponents and likely correspond to the same universality class.

V. SCALING THEORETICAL ARGUMENTS

In the following, we develop a scaling theory that connects dynamical heterogeneities observed in finite-temperature simulations (Sec. III) and the zero-temperature critical point, and associated avalanches, of the extremal dynamics (Sec. IV). We also discuss other important physical consequences, such as the time evolution of avalanche sizes and the Stokes-Einstein violation.

A. Length scale of dynamical heterogeneity

We consider the effect of finite temperature T on the extremal dynamics. As we discuss below, the breakdown of the condition for the extremal dynamics naturally leads to

the length scale ξ of dynamical heterogeneity at finite T. The proposed picture is schematically depicted in Fig. 8.

At finite but low T, the dynamics is expected to be extremal on large but finite length scales. To understand the underlying mechanism, let us consider a finite-size system. For a fixed system size, if T is small enough, the site with the lowest activation energy $E_{\min}$ typically relaxes first like for $T = 0^+$ (the probability to relax the site with the second-lowest energy is negligible). This relaxation corresponds to a slow "nucleation" event when $E_{\min} \approx E_c$ that occurs on a timescale $\tau_\alpha \sim e^{E_c/T}$, as schematically shown in Fig. 8(a). The nucleation event lowers energy barriers of some other sites of the system, which we call "facilitated" sites, due to elastic interactions, and causing a sequence of faster events when $E_{\min} < E_c$, as shown in Fig. 8(b). This cascade process forms an avalanche, which eventually stops. A new avalanche starts again once another nucleation event occurs. The dynamics is, thus, intermittent with the power-law avalanches discussed in Sec. IV. Clearly, there is a typical size N_T above which this picture breaks down. Indeed, the above description holds when the thermal energy T is much smaller than the typical energy difference between the lowest and second-lowest activation energies, $\langle E_{\text{second}} - E_{\min} \rangle$; otherwise, sites with higher energy barriers (such as E_{second}) might relax and dynamics cease to be extremal. According to Eq. (4), $\langle E_{\text{second}} - E_{\min} \rangle$ depends on the system size N. Thus, the condition for the extremal dynamics which interplays T and N is given by $T \ll \langle E_{\text{second}} - E_{\min} \rangle \sim N^{-\delta}$, i.e., $N \ll N_T \sim T^{-1/\delta}$.

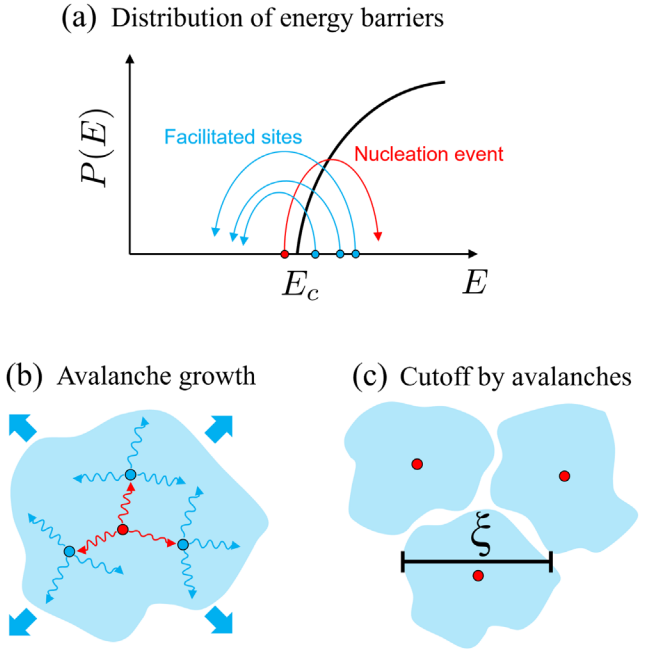

FIG. 8. Proposed picture for dynamical heterogeneities in glass-forming liquids. (a) At low temperatures, the distribution of activation energy barriers $P(E)$ presents a gap below some energy E_c. On a timescale $\tau_\alpha \sim e^{E_c/T}$, a site with a barrier near E_c relaxes (red arrow), which we call a "nucleation event." As a result, due to elastic interactions, other sites may display lower barriers $E < E_c$ (blue arrows), which we call "facilitated sites." They relax on a timescale much faster than τ_α, leading to a rapid sequence of events, forming a thermal avalanche. The corresponding real space picture is shown in (b) and (c). (b) A nucleation event (red circle) triggers facilitated sites (blue circles) by elastic interactions (wavy arrows). These induced events again induce other sites, forming an avalanche growth. (c) Avalanche growth is cut off due to other avalanches originating from different nucleation events taking place simultaneously in the system. The cutoff length ξ corresponds to the maximum size for which extremal dynamics applies, which defines the length of dynamical heterogeneity at finite temperature.

In consequence, when the system size N is too large at fixed T, the above description cannot hold. In this case, in particular in the thermodynamic limit, multiple nucleation events followed by avalanches take place (independently) in parallel in the system, as sketched in Fig. 8(c). The cutoff length scale ξ encompassing a single avalanche is not limited by system size but by other avalanches in the system, which can be estimated assuming that the locations of these avalanches are independent. Such an approximation will be accurate if structural spatial correlations are not preponderant in this system, as discussed below. Assuming finite-size scaling, ξ^d must then correspond to the largest system size N_T for which extremal dynamics at finite T holds, i.e., $\xi^d \sim N_T$. This provides the link between finite-size zero-temperature avalanches and thermal ones. Moreover, it also directly predicts that the size of dynamically correlated regions characterized by χ_4^*, which is given by the crossover size above which the condition for the extremal dynamics breaks down: $\chi_4^* \sim \xi^{\tilde{d}_f}$ leading to $\chi_4^* \sim T^{-\tilde{d}_f/d\delta}$. In conclusion, we derive two scaling relations for thermal avalanches:

$$\gamma = \frac{\tilde{d}_f}{d\delta}, \tag{5}$$

$$\nu = \frac{1}{d\delta}. \tag{6}$$

These scaling relations connect dynamical heterogeneities at finite T (characterized by γ and ν) and the distribution of local energy barriers at $T = 0^+$ (characterized by δ) together with the morphology of avalanches during the extremal dynamics (by $\tilde{d}_f$). We thus predict γ and ν by using δ and $\tilde{d}_f$ measured in the extremal dynamics in Sec. IV. These predictions are in good agreement with finite-temperature simulations in Sec. III, as summarized in Table I. We also find that the mean-field predictions using $\delta_{\text{MF}} = 2/3$ and $\tilde{d}_f = d = 2$ lead to similar values.

This argument is expected to break down if large spatial correlations characterize the structure of the system, causing the locations where avalanches start to be correlated.

Indeed, as is always the case in disordered materials at zero temperature, any critical threshold such as x_c or E_c must display finite-size fluctuations $\Delta x_c \sim \Delta E_c$. These fluctuations are described by some exponent ν', such that, in a system of finite size L, one has $\Delta E_c \sim L^{-1/\nu'}$. The value of ν' is affected by spatial correlations. In general, one must have $\nu' \geq \nu$, since the fluctuations of Δx_c or ΔE_c must be at least as large as the typical distance between most unstable sites in a quiescent system $E_{\text{second}} - E_{\text{min}} \sim L^{-1/\nu}$: Indeed, E_c cannot be more precisely defined than this difference. We expect our argument above to hold when $\nu = \nu'$, corresponding to $\Delta E_c \sim E_{\text{second}} - E_{\text{min}}$. ν' can be related to previously introduced exponents $1/\tilde{\sigma}$ and $\tilde{d}_f$ as follows. If a finite system displays a system-spanning avalanche $\tilde{S} \sim \tilde{S}_c \sim L^{\tilde{d}_f}$ and entirely rearranges, then the change of x_c, or equivalently that of E_c, must be of the order of Δx_c. According to Eq. (3), an avalanche of size $\tilde{S} \sim \tilde{S}_c \sim L^{\tilde{d}_f}$ is associated with a characteristic change of the critical threshold $\Delta x_c = x_c - x_0 \sim L^{-\tilde{\sigma}\tilde{d}_f}$ [when $z \approx 1$ in $f(z)$], implying that $\xi \sim \Delta x_c^{-1/(\tilde{\sigma}\tilde{d}_f)}$. Since $\Delta x_c \sim \Delta E_c$ and $\Delta E_c \sim \xi^{-1/\nu'}$, we obtain $\nu' = 1/(\tilde{\sigma}\tilde{d}_f)$. Using numerical values for $\tilde{\sigma}$ and $\tilde{d}_f$, this expression leads to $\nu' \approx 0.95$ and $\nu' \approx 0.9$, respectively, for the scalar and tensorial models. We, thus, have in the present system $\nu \approx \nu'$, supporting our assumption of independent avalanches. Note, however, that such an equality does not need to hold, in general, especially in large d.

B. Time evolution of thermal avalanches

We now focus on the time evolution of the size of thermal avalanches, based on the scaling results for the extremal dynamics. In Sec. IV, we introduce x_0 avalanches to more generally probe the critical behavior at $x_0 = x_c$. This turns out to be useful also to work out the relationship between time and length scales for thermal avalanches. In fact, x_0 is associated to a typical energy scale $E(x_0) = x_0^{3/2}$. Hence, it carries information both about the typical timescale $\tau(x_0) \sim e^{E(x_0)/T}$ and the avalanche (cutoff) size $\tilde{S}_c(x_0)$.

According to the scaling argument discussed before, even at a finite temperature T, the extremal dynamics can be applied to a finite system, in particular, smaller than N_T. The cutoff size of x_0 avalanches, $\tilde{S}_c$, follows $\tilde{S}_c \sim (x_c - x_0)^{-1/\tilde{\sigma}}$; see Eq. (3) and Fig. 5(b). During an extremal dynamics, the duration of an avalanche is dominated by the relaxation of the most stable site it involves, of characteristic timescale $\tau(x_0) \sim e^{E(x_0)/T}$. We, thus, obtain a relation connecting the duration of avalanches, $\tau(x_0)$ (measured in the unit of the relaxation time $\tau_\alpha \sim e^{E_c/T}$), with the cutoff size $\tilde{S}_c$ as $\tilde{S}_c^{-\tilde{\sigma}} \sim (x_c - x_0) \sim E_c - E(x_0) \sim T \ln[\tau_\alpha/\tau(x_0)]$. Therefore, avalanches in such a finite system and over a finite time interval t (smaller than the relaxation timescale τ_α) are intermittent. Namely, the system is quiescent most of the time, yet when it is not, its avalanche size $\tilde{S}(t)$ is power-law distributed with a cutoff size $\tilde{S}_c(t)$, which is given by

$$\tilde{S}_c(t) \sim [T \ln(\tau_\alpha/t)]^{-1/\tilde{\sigma}}. \tag{7}$$

Thus, we find that the size of avalanches grows very slowly—only logarithmically—with time.

The above prediction can be tested experimentally or in molecular dynamics simulations [43,52]. In Ref. [52], the time evolution of a chord length $\langle \ell \rangle$ characterizing the linear size of mobile domains has been measured. Since we expect $\tilde{S}_c \sim \langle \ell \rangle^{\tilde{d}_f}$, our prediction for $\langle \ell \rangle$ is given by

$$\langle \ell \rangle^{\text{Pred}} = A(T)[T \ln(\tau_\alpha/t)]^{-1/(\tilde{\sigma}\tilde{d}_f)}, \tag{8}$$

where $A(T)$ is a function with a finite limiting value as $T \to 0$. In Fig. 9, we compare the molecular simulation data for a two-dimensional polydisperse mixture [52] and our prediction. The prediction is very good, in particular, at lower temperatures where the elastoplastic description is supposed to work well.

In Appendix B, we also connect $\tilde{S}_c(t)$ and $\chi_4(t)$ explicitly. This allows us to predict the time evolution of $\chi_4(t)$ for times $1 \ll t \ll \tau_\alpha$—a prediction that agrees with the numerics.

C. Decoupling between diffusion and relaxation

We now show that the scaling theory developed above directly implies decoupling between diffusion and

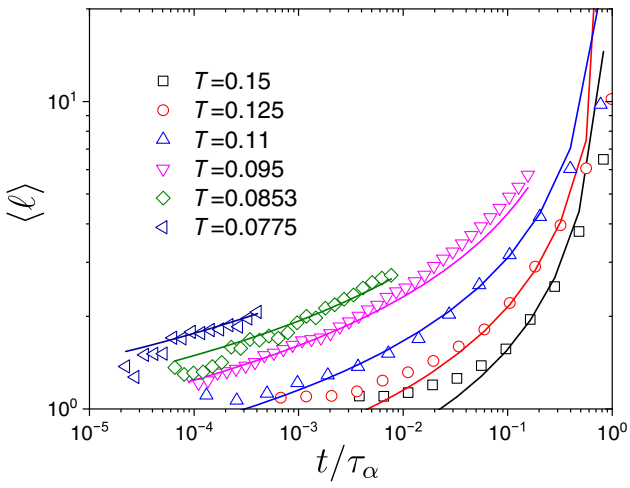

FIG. 9. Comparison between the molecular simulation data (empty points) in Ref. [52] and our theoretical prediction (solid curves) in Eq. (8) for the time evolution of a linear avalanche size $\langle \ell \rangle$. We set $1/\tilde{\sigma} = 1.8$ and $\tilde{d}_f = 2$, based on Table II. We use $A = 0.6$, 0.7, 0.9, 1.1, 1.2, and 1.3 for $T = 0.15$, 0.125, 0.11, 0.095, 0.0853, and 0.0775, respectively.

relaxation as found in supercooled liquids, the so-called Stokes-Einstein violation [53–57].

One of the remarkable aspects found in the numerical simulations in Sec. IV is that sites relax *multiple times* within the same avalanche. In terms of a dynamical trajectory, a site waits a long time (remains immobile) before relaxing, but once it relaxes, it redoes multiple times within a short period of time. This is characterized by a difference between the so-called persistence time and exchange time [58–60] (or the caging time in molecular simulations [62,91]), which has been argued to be the key ingredient of decoupling between diffusion and relaxation in supercooled liquids [58–62].

In our case, this effect originates from the difference between the event-based and site-based avalanche sizes characterized by $d_f > \tilde{d}_f$. To connect it to the zero-temperature critical point, let us focus on the formation of a thermal avalanche whose timescale is the order of τ_α and linear size is ξ. During the formation, a single site relaxes of the order of $\xi^{d_f}/\xi^{\tilde{d}_f}$ times. Assuming that each relaxation gives a random displacement to particles in the neighborhood of this site, their diffusion constant D must be proportional to the rate for the relaxation event, $\xi^{(d_f-\widetilde{d_f})}/\tau_\alpha$, leading to a Stoke-Einstein breakdown $D\tau_\alpha$ of the order of $D\tau_\alpha \sim \xi^{(d_f-\widetilde{d_f})} \sim T^{-h}$ that diverges at vanishing temperature with $h = \nu(d_f - \widetilde{d_f})$. Conventionally, the Stokes-Einstein violation is considered a consequence of spatially heterogeneous dynamics [54]. We directly connect the former and the length scale of dynamical heterogeneity ξ. On top of that, our scaling theory emphasizes accumulations of multiple events inside a mobile region as the microscopic mechanism leading to the Stokes-Einstein violation.

Note that our scaling argument does not predict a fractional Stokes-Einstein violation in which $D \sim \tau_\alpha^{-\zeta}$, or $D\tau_\alpha \sim \tau_\alpha^{1-\zeta}$, but instead $D\tau_\alpha \sim (\log \tau_\alpha)^{1-\zeta'}$ where $1-\zeta' = \nu(d_f - \tilde{d}_f)$. The former is the fit that is usually conjectured from experimental data [92,93] with $\zeta \approx 0.8$. However, given the small value of $1-\zeta$, the latter fit is also a viable option [94].

We numerically test our prediction for the Stokes-Einstein violation in Fig. 10, showing the product $D\tau_\alpha$ in the tensorial model. In this plot, D is estimated numerically using tracer particles that jump randomly by one lattice spacing each time relaxation occurs in their current site, similarly to what was originally done for kinetic constrained models [58,59] (see Appendix B for details). $D\tau_\alpha$ increases with decreasing T, following the scaling prediction $D\tau_\alpha \sim T^{-h}$ with $h = \nu(d_f - \tilde{d}_f)$ measured independently in Secs. III and IV. The observed amount of the violation we find is not large and, hence, more representative of strong glass-forming liquids than fragile ones, since it has been reported that the magnitude of the violation and fragility are correlated [54,97]. We come back to this point in Sec. VI.

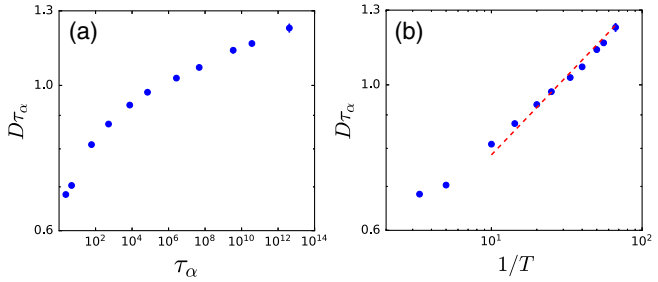

FIG. 10. The Stoke-Einstein decoupling $D\tau_\alpha$, where D is the diffusion coefficient of tracers, for the tensorial elastoplastic model with $L = 128$. (a) $D\tau_\alpha$ versus τ_α could suggest an effective power-law behavior (the fractional Stokes-Einstein violation), with two apparent exponents in the range $\tau_\alpha < 10^4$ and $\tau_\alpha > 10^4$. (b) Our prediction suggests instead a power-law behavior in terms of T. The red dashed line represents $D\tau_\alpha \sim T^{-\nu(d_f-\tilde{d}_f)}$.

VI. CONCLUSION AND DISCUSSION

We provided a theoretical description of dynamical heterogeneities in supercooled liquids based on the assumption that local rearrangements are elastically coupled. The elastoplastic models we studied offer a quantitative solution for how dynamical correlations can emerge even in cases in which local barriers control the dynamics [19,22,33,98,99]. Our main result is the theoretical explanation of dynamical correlations in terms of a zero-temperature critical point with the associated scaling relations. This leads to quantitative predictions on the power-law statistics of thermal avalanches testable in more realistic systems. Our study suggests that dynamical heterogeneities in supercooled liquids should be investigated in terms of the temperature T to seek power-law relations rather than in terms of the relaxation timescale.

One important aspect of the models we studied is that they encode in a very simple and natural way the coupling of local relaxation and elastic interaction. Their simplicity, combined with the richness of the dynamical behavior—in particular, the emergence of facilitation and dynamical correlations—is a remarkable aspect, as it shows which salient facts one can obtain with minimal physical ingredients (see also previous mesoscopic modelings leading to dynamical facilitation [100–102]). Kinetically constrained models have instead abstract kinetic rules and show a large variety of behaviors depending on the kinetic constraints [13]. Although local excitations identified in the dynamic facilitation scenario [44,103] would have connections with local activations in our framework, the physical interpretation of kinetic rules in kinetic constrained models is still an open and crucial challenge. Along this line of thought, it would be interesting to devise a kinetic constraint rule effectively incorporating elastoplasticity. Nevertheless,

various concepts and theoretical tools developed in the study of kinetically constrained models provide important guidelines and, in fact, played an essential role for our analysis of thermal elastoplastic models. It has been demonstrated in the dynamic facilitation theory that a critical point in an extended nonequilibrium phase diagram influences glassy dynamics [104,105]. It would also be interesting to study whether such a critical point exists in elastoplastic models.

Quantitatively, the magnitude of dynamical heterogeneities we simulated is comparable to most supercooled liquids (as the estimated χ_4^* increases by about two decades as the glass transition is reached [7,74]), whereas the magnitude of the Stoke-Einstein breakdown is comparable to that of rather strong glass-forming liquids [54]. According to our scaling argument, such a breakdown will increase if the system shows more intensive accumulations of multiple relaxations characterized by larger $\nu(d_f - \tilde{d}_f)$. This effect could be achieved by imposing that some of the model parameters (such as the local values of the yield stress, or how sites are coupled to the elastic field) are randomly distributed [106] instead of being single valued as assumed here for simplicity. These effects are expected in glass-forming liquids due to the presence of structural heterogeneity of local orders [107–110]. Such generalization would allow us to study the structure-dynamics relationship [111–113] in elastoplastic models. Further improvements may be achieved by adding fluctuations and nonlinearities to the propagator, which are present at short range [114,115]. An interesting line of research to develop quantitative models is a mapping from a molecular simulation to an elastoplastic model [116–118] or the one pursued in Refs. [119,120], which uses machine learning methods and the so-called softness field to obtain quantitative effective models.

Our results also underline important themes to study in the future, including the nature of local rearrangements in glass-forming liquids and their connection to fragility [2]. Concerning the latter, the current elastoplastic models correspond to strong glass formers with Arrhenius behavior, with activation energy given by the magnitude of the gap E_c entering the distribution of local barriers [35,42]. This point results from the simplifying assumption that the energy scale of local rearrangements does not vary with temperature. In an improved (still simplified) model where all elastic energies follow the high-frequency elastic modulus $G_\infty(T)$ of the material, the activation energy E_c will be proportional to $G_\infty(T)$, a correlation known to exist in some glass-forming liquids [19,121]. More recent works relate this energy scale of local rearrangements to local (or nonlocal) elasticity [21], plasticity [33], or alternatively the varying geometry of elementary rearrangements under cooling [122]. Local energy barriers could also be affected by locally favored structures [108,123]. More progress along those lines will be instrumental to understand what controls fragility in glass-forming liquids.

Note that, although we mainly focused our attention on the theoretical scenario based on local barriers driving the dynamics [21,22,33] together with facilitation and avalanches, the physical phenomena discussed in this work are more general. For example, they can also apply to cases in which cooperative rearrangements take place. In these perspectives, in particular, within random first-order transition theory, the local relaxation event would correspond to a cooperative rearrangement [52,124]. Obviously, our current elastoplastic models do not take into account growing cooperativity as a static correlation, and they have a singularity only at $T = 0$ in contrast to random first order transition theory with a finite-temperature singularity at $T_K > 0$. One could incorporate a growing static correlation in the models by increasing the number of sites involving a thermal activation process. It would be interesting to work out precise predictions in this case.

Finally, we expect our scaling theory which connects spatial correlations at finite temperature to extremal dynamics at zero temperature, to be relevant for a broader class of problems beyond the context of the glass transition studied here. Phenomena in which the implications of these arguments could be studied include the creep flow of disordered materials [125–131] or that of pinned elastic interfaces [48,132,133] below the threshold force where they spontaneously flow.

ACKNOWLEDGMENTS

We thank the Simons Collaboration for discussions, in particular, J. Baron, L. Berthier, C. Brito, C. Gavazzoni, E. Lerner, C. Liu, D. R. Reichman, and C. Scalliet. We thank S. Patinet for insightful discussions. We appreciate C. Scalliet for sharing the data in Ref. [52]. G. B. thanks J. P. Bouchaud for discussions, in particular, on the Bak-Sneppen model and models of dynamic facilitation. M. W. thanks A. Rosso and M. Muller for discussions on avalanche-type response over the years and T. de Geus, W. Ji, and M. Pica Ciamarra for discussions. M. W. acknowledges support from the Simons Foundation Grant (No. 454953 Matthieu Wyart) and from the SNSF under Grant No. 200021-165509. G. B. acknowledges support from the Simons Foundation Grant (No. 454935 Giulio Biroli).

APPENDIX A: THERMAL ELASTOPLASTIC MODELS

1. Scalar model

We study a scalar elastoplastic model [35] in a two-dimensional lattice whose linear box length is L using the lattice constant as the unit of length. For each site, we assign local shear stress σ_i (scalar variable) at a position $\mathbf{r}_i$.

The dynamical rule for the simulation model is akin to Monte Carlo dynamics [134]. We pick a site, say, i, up

randomly among L^2 sites. If σ_i is greater (or lower) than or equal to a threshold $\sigma_Y > 0$ (or $-\sigma_Y < 0$), namely, $|\sigma_i| \geq \sigma_Y$, this site shows a plastic event: $\sigma_i \to \sigma_i - \delta\sigma_i$, where $\delta\sigma_i$ is the local stress drop. We use an uniform threshold, $\sigma_Y = 1$. Instead, if $|\sigma_i| < \sigma_Y$, with probability $e^{-E(\sigma_i)/T}$, where $E(\sigma_i)$ is a local energy barrier and T is the temperature, this site shows a plastic event: $\sigma_i \to \sigma_i - \delta\sigma_i$. This corresponds to a plastic rearrangement induced by a local thermal activation. We employ $E(\sigma_i) = (\sigma_Y - |\sigma_i|)^\alpha$ with $\alpha = 3/2$ [135]. By introducing the local stress distance to threshold, $x_i = \sigma_Y - |\sigma_i|$, we can rewrite $E(x) = x^{3/2}$. This specific form of the local energy barrier is suggested by molecular simulation studies [33,68] and previous elastoplastic models under shear [42,66]. The stress drop $\delta\sigma_i$ associated with a plastic event is a stochastic variable. In this paper, we use $\delta\sigma_i = (z + |\sigma_i| - \sigma_Y)\mathrm{sgn}(\sigma_i)$, where $\mathrm{sgn}(x)$ is the sign function and $z > 0$ is a random number drawn by an exponential distribution, $p(z) = (1/z_0)e^{-z/z_0}$. z_0 is the mean value, and we set $z_0 = 1$. This exponential distribution would be realistic according to molecular simulations in Ref. [136].

A local plastic event at site i influences all other sites ($\forall\ j \neq i$) as

$$\sigma_j \to \sigma_j + G^{\psi_i}_{\mathbf{r}_{ji}}\delta\sigma_i, \tag{A1}$$

where $\mathbf{r}_{ji} = \mathbf{r}_j - \mathbf{r}_i$ and $\psi_i \in [0, \pi/2)$ is a random orientation of the Eshelby kernel $G^{\psi}_{\mathbf{r}}$. Numerical implementation of $G^{\psi}_{\mathbf{r}}$ is described in Ref. [35].

Similar to the Monte Carlo dynamics, we repeat the above attempt L^2 times, which corresponds to unit time.

For the initial condition, we draw the local stress σ_i ($\forall\ i$) randomly while keeping the force balance; i.e., the sum of stresses along each row and column of lattice sites is strictly zero [137,138]. To study dynamical properties at the steady state, we monitor the waiting time dependence of observables, and we report them only at the steady state, discarding the initial transient part.

2. Tensorial model

We implement a two-dimensional elastoplastic model in which we account for the tensorial nature of the shear stress tensor. In this tensorial version of the elastoplastic model, the state of each site i is described by its local shear stress tensor $\tilde{\sigma}_i$. Note that symbols σ and $\tilde{\sigma}$ are also used as critical exponents in the main text, not to be confused with local shear stress defined here. The shear stress tensor is traceless and symmetric, and, hence, in two dimensions it is defined by two independent components: $\tilde{\sigma}_{xx,i}$ and $\tilde{\sigma}_{xy,i}$.

The local yield stress is defined by a surface in the shear stress space, with the region inside and outside the surface corresponding to mechanically stable (elastic, immobile) and unstable (plastic, mobile) states, respectively. The minimum amount of shear stress required to make a site unstable is the distance to the yield surface, and we denote its magnitude by x, as schematically shown in Fig. 11. We choose the local yield surface to consist of two parallel lines at an angle θ_Y with respect to the $\tilde{\sigma}_{xx}$ axis in shear stress space, centered at zero shear stress and separated by $2\sigma_Y$ (see Fig. 11). The local yield surface is assigned for each site i. We initiate $\theta_{Y,i}$ with a uniformly distributed random number in $[0, 2\pi)$.

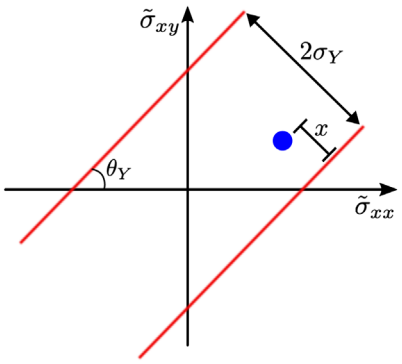

FIG. 11. A schematic plot of the yield surface for the tensorial model. The blue dot shows the state of a site in the shear stress space. The yield surface is described by two parallel lines separated by $2\sigma_Y$, and each line makes an angle of θ_Y with the $\tilde{\sigma}_{xx}$ axis. The distance from the yield surface is shown by x.

When a site i becomes unstable, it undergoes a plastic event over a timescale τ_0: $\tilde{\sigma}_{xx,i} \to \tilde{\sigma}_{xx,i} - \delta\tilde{\sigma}_{xx,i}$ and $\tilde{\sigma}_{xy,i} \to \tilde{\sigma}_{xy,i} - \delta\tilde{\sigma}_{xy,i}$, where the amount of stress drops $\delta\tilde{\sigma}_{xx,i}$ and $\delta\tilde{\sigma}_{xy,i}$ are given by

$$\delta\tilde{\sigma}_{xx,i} = -(z - x)\ \sin(\theta_{Y,i})\,\mathrm{sgn}(\tilde{\sigma}_{xx,i}), \tag{A2}$$

$$\delta\tilde{\sigma}_{xy,i} = -(z - x)\ \cos(\theta_{Y,i})\,\mathrm{sgn}(\tilde{\sigma}_{xy,i}), \tag{A3}$$

respectively. $\mathrm{sgn}(x)$ is the sign function, and z is a random number drawn from an exponential distribution $p(z) = e^{-z/z_0}/z_0$ with $z_0 = 1$. The duration of a plastic event τ_0 is accounted for by triggering the relaxation with a probability per unit time $1/\tau_0$ whenever the site is unstable. In an athermal system, sites can relax only by first becoming unstable. At finite temperature T, stable sites undergo relaxation at the rate $e^{-E(x)/T}/\tau_0$, where $E(x) = x^{3/2}$ is the local energy barrier [42]. After each plastic event, we redraw the angle of the yield surface $\theta_{Y,i}$ from a uniform random distribution.

Note that to simulate such a dynamics at low temperatures we implement a Gillespie type of algorithm [42], which operates as follows. Consider an event occurring at some time t. Following it, a relaxation time τ_i for each site i is chosen with an exponential distribution of mean $e^{-E(x_i)/T}/\tau_0$. The next event corresponds to the smallest τ_i, leading to a plastic event on the corresponding site, which occurs at a time $t + \tau_i$. At that point, stresses are computed

once again, and the variables τ_i are sampled from their new distributions. This algorithm is then repeated iteratively.

To maintain the force balance, a plastic event at site i redistributes the shear stress field in the other sites following the force dipole propagator. In Fourier space, the elements of elastic kernel are given by

$$\hat{G}_{xx,xx}(\mathbf{q}) = -\frac{(q_x^2 - q_y^2)^2}{(q_x^2 + q_y^2)^2}, \tag{A4}$$

$$\hat{G}_{xy,xy}(\mathbf{q}) = -\frac{4q_x^2 q_y^2}{(q_x^2 + q_y^2)^2}, \tag{A5}$$

$$\hat{G}_{xx,xy}(\mathbf{q}) = \hat{G}_{xy,xx}(\mathbf{q}) = -\frac{2q_x q_y (q_x^2 - q_y^2)}{(q_x^2 + q_y^2)^2}, \tag{A6}$$

where $\mathbf{q} = (q_x, q_y)$ is the Fourier vector. For a discrete system with periodic boundary conditions, we introduce a correction term to the Fourier modes, given by $q_x^2 = 2 - 2\cos(2\pi n_x/L)$, $q_y^2 = 2 - 2\cos(2\pi n_y/L)$, and $q_x q_y = 2\sin(2\pi n_x/L)\sin(2\pi n_y/)$, where $n_\alpha = -L/2 + \{1, \ldots, L\}$ with $\alpha = x, y$.

APPENDIX B: CHARACTERIZATIONS OF DYNAMICAL HETEROGENEITIES FOR FINITE-TEMPERATURE SIMULATIONS

1. Four-point correlation function

We explain how to analyze correlation functions for finite-temperature simulations. We first consider the persistence two-point time correlation function $\langle \pi(t) \rangle_{\text{time}}$, which is defined by $\pi(t) = (1/L^d)\sum_i p_i(t)$, where $p_i(t) = 1$ (immobile) if the site i does not show a plastic event until time t from $t = 0$ and $p_i(t) = 0$ (mobile) otherwise. $\langle \cdots \rangle_{\text{time}}$ denotes the time average at the stationary state. $\langle \pi(t) \rangle_{\text{time}}$ for the scalar and tensorial models are presented in Fig. 1 in Ref. [35] and Fig. 1(a) in the main text, respectively. We then measure a four-point correlation function $\chi_4(t)$, defined by

$$\chi_4(t) = L^d(\langle \pi^2(t) \rangle_{\text{time}} - \langle \pi(t) \rangle_{\text{time}}^2). \tag{B1}$$

$\chi_4(t)$ for the scalar and tensorial models are presented in Fig. 3 in Ref. [35] and Fig. 2(b) in the main text, respectively. $\chi_4(t)$ quantifies the size of the dynamically correlated region, because one can rewrite it as

$$\chi_4(t) = \frac{1}{L^d}\sum_{i,j}(\langle p_i(t)p_j(t) \rangle_{\text{time}} - \langle \pi(t) \rangle_{\text{time}}^2) \tag{B2}$$

$$= \frac{1}{L^d}\sum_i \sum_k \langle \phi_i(t)\phi_{i+k}(t) \rangle_{\text{time}}, \tag{B3}$$

where $\phi_i(t) = p_i(t) - \langle \pi(t) \rangle_{\text{time}}$. For example, $\phi_i(\tau_\alpha) = \pm 1/2$. Therefore, $\chi_4(t)$ is proportional to the average number of sites correlated dynamically. Therefore, its peak value χ_4^* contains essentially the same information as $\tilde{S}$; in particular, $\chi_4^* \sim \tilde{S}_c$ at $T = 0^+$.

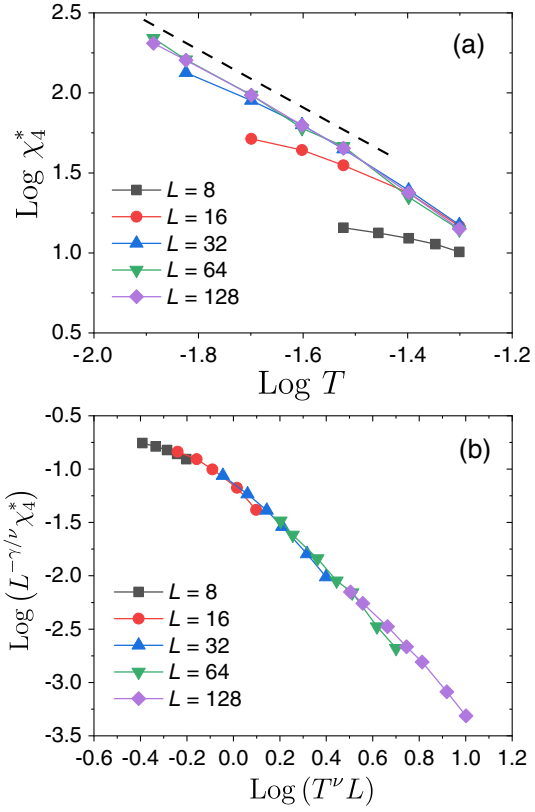

FIG. 12. The four-point correlation function χ_4 for the scalar model. (a) The peak value χ_4^* versus T for several L in a log-log plot. The dashed line follows $\chi_4^* \sim T^{-\gamma}$. (b) Scaling collapse of $\chi_4^*(L, T)$, which determines ν.

Figure 12(a) shows χ_4^* versus T for several system sizes L for the scalar model. One can see a scaling regime $\chi_4^* \sim T^{-\gamma}$ at lower T and larger L. A scaling collapse is obtained in Fig. 12(b), which determines another critical exponent ν associated with a length scale of dynamical heterogeneity. The obtained values for the critical exponents are reported in Table II.

2. Dynamical correlation length scale

We consider extracting a correlation length directly instead of performing finite-size scaling. To this end, we measure the spatial dependence of the four-point structure factor $S_4(q, t)$ [78], defined by

$$S_4(q, t) = \frac{1}{L^d}\sum_{ij}(\langle p_i(t)p_j(t) \rangle_{\text{time}} - \langle \pi(t) \rangle_{\text{time}}^2) e^{i\mathbf{q}\cdot(\mathbf{r}_i - \mathbf{r}_j)}, \tag{B4}$$

where $q = |\mathbf{q}|$. In Fig. 13(a), we show $S_4(q, t)$ for the scalar model at $t = \tau^*$ when $\chi_4(t)$ takes the peak value

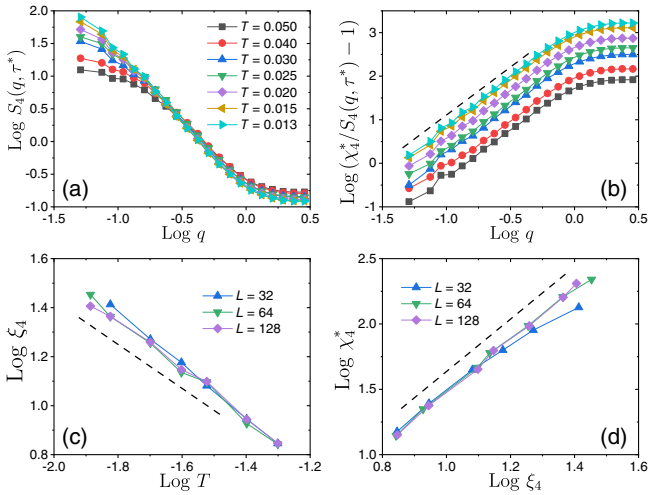

FIG. 13. The four-point structure factor $S_4(q,t)$ and the associated correlation length ξ_4 for the scalar model. (a) $S_4(q,\tau^*)$ for several temperatures for $L=128$. (b) The corresponding plot for the Ornstein-Zernike form in Eq. (B5). The dashed line defines a slope corresponding to the exponent a. (c) The extracted ξ_4 versus T. The dashed line follows $\xi_4 \sim T^{-\nu}$. (d) χ_4^* versus ξ_4. The dashed line follows $\chi_4^* \sim \xi_4^{\tilde{d}_f}$.

$\chi_4^* = \chi_4(\tau^*)$. We find that τ^* is close to τ_α, and, thus, $S_4(q,\tau^*)$ encodes heterogeneity associated with structural relaxation. We note that, at the long wavelength limit, $S_4(q,t)$ converges to $\chi_4(t)$, namely, $\lim_{q\to 0} S_4(q,t) = \chi_4(t)$. We then assume the Ornstein-Zernike form at lower q:

$$S_4(q,\tau^*) = \frac{\chi_4^*}{1+(q\xi_4)^a}, \tag{B5}$$

where ξ_4 is the dynamical correlation length extracted and a is an exponent. As shown in Fig. 13(b), we find this scaling with $a = 2.2$. From this plot, we extract ξ_4 and present its temperature dependence in Fig. 13(c). This analysis can be done only for larger systems, $L = 32$, 64, and 128, since the scaling regime cannot be reached in smaller systems within our simulations. We find $\xi_4 \sim T^{-\nu}$ with $\nu = 0.9$, which is consistent with the one estimated from the finite-size scaling in Fig. 12. Moreover, the χ_4^* versus ξ_4 plot [139,140] in Fig. 13(d) provides us with the fractal dimensions, $\tilde{d}_f = 2$, which is also consistent with the one measured in the extremal dynamics in Fig. 18.

3. Prediction for the four-point correlation function

We connect the cutoff size for the site-based avalanche size, $\tilde{S}_c(t)$, in a given time interval t and the time evolution of the four-point correlation function $\chi_4(t)$.

We first compute the site-based avalanche size by $\tilde{S}(t) = \sum_{i=1}^{N} n_i(t)$, where $n_i(t) = 0$ if the site i does not exhibit a plastic event until time t and $n_i(t) = 1$ for mobile sites that relax at least once. Thus, $n_i(t)$ can be written by $n_i(t) = 1 - p_i(t)$. The first and second moments of $\tilde{S}(t)$ measured by the time average are given by

$$\langle \tilde{S}(t)\rangle_{\rm time} = N[1 - \langle \pi(t)\rangle_{\rm time}],$$
$$\langle \tilde{S}^2(t)\rangle_{\rm time} = \sum_{i,j}\Big\{\langle p_i(t)p_j(t)\rangle_{\rm time} - [2\langle \pi(t)\rangle_{\rm time} - 1]\Big\},$$

respectively. Consider a correlation volume of linear extension ξ. On this length scale, $\chi_4(t)$ crosses over toward its value for an infinite system. It is also the largest length for which extremal dynamics applies, implying that $\tilde{S}(t)$ is distributed in a power-law fashion. Thus, $\tilde{S}_c(t)$ can be estimated by $\langle \tilde{S}^2(t)\rangle_{\rm time}/\langle \tilde{S}(t)\rangle_{\rm time}$, as given by

$$\tilde{S}_c(t) = \frac{\sum_{i,j}\{\langle p_i(t)p_j(t)\rangle_{\rm time} - [2\langle \pi(t)\rangle_{\rm time} - 1]\}}{N[1 - \langle \pi(t)\rangle_{\rm time}]}. \tag{B6}$$

In general, one can expect that $\langle \pi(t)\rangle_{\rm time}$ follows the (stretched) exponential decay, $\langle \pi(t)\rangle_{\rm time} \simeq e^{-(t/\tau_\alpha)^\beta}$, where β is an exponent. Typically, $0 < \beta \le 1$ for equilibrium supercooled liquids. Our elastoplastic models show nearly exponential relaxation with $\beta \simeq 1$. We now consider the early time stage, where $\langle \pi(t)\rangle_{\rm time}$ can be approximated by $\langle \pi(t)\rangle_{\rm time} \simeq 1 - (t/\tau_\alpha)^\beta$. Under such a circumstance, Eq. (B6) and $\chi_4(t)$ defined in Eq. (B2) suggest that $\tilde{S}_c(t) \simeq (t/\tau_\alpha)^{-\beta}\chi_4(t)$. Together with Eq. (7) in the main text, we predict the time evolution of $\chi_4(t)$ as

$$\chi_4(t) \simeq A(t/\tau_\alpha)^\beta [T\,\ln(\tau_\alpha/t)]^{-1/\tilde{\sigma}}, \tag{B7}$$

where A is a constant which does not depend on t and T.

Figure 14(a) shows a log-log plot for $\chi_4(t)$ measured at finite-temperature simulations for the scalar model. The initial growth can be fitted effectively by a power law, $\chi_4(t) \sim t^b$ [141,142], with $b \simeq 1.4$. Instead, our argument in Eq. (B7) predicts a linear growth with a logarithmic correction. In Fig. 14(b), we show a parametric plot to numerically test Eq. (B7) with $\beta = 1$, $A = 0.5$, and $1/\tilde{\sigma} = 1.9$ (see Table II). We find that the simulated $\chi_4(t)$ for different temperatures follows our prediction at early times. Deviations from the prediction can be observed on

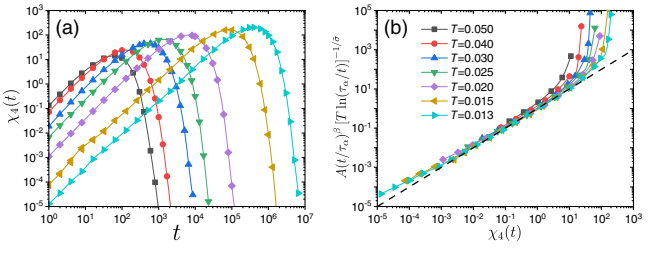

FIG. 14. (a) Log-log plot for $\chi_4(t)$ for the scalar model with $L = 128$ for $T = 0.050$, 0.040, 0.030, 0.025, 0.020, 0.015, and 0.013 (from left to right). (b) Parametric plot to test the prediction in Eq. (B7). The dashed line defines the linear relation.

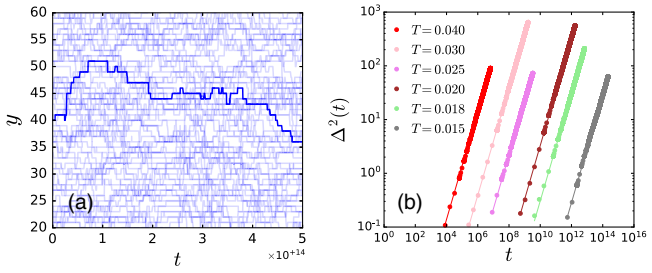

FIG. 15. Diffusion of tracer particles for the tensorial model with $L = 128$. (a) The y component of typical trajectory of a tracer particle with $T = 0.015$ ($\tau_\alpha = 4.14 \times 10^{12}$). (b) Mean-squared displacement $\Delta^2(t)$ of tracer particles are shown with points. The solid lines follow $\Delta^2(t) = Dt$, from which we extract the diffusion coefficient D.

very short timescales. This is presumably due to the fact that, on such timescales, the corresponding energy scale is too small compared with E_c, which violates the assumption underlying the asymptotic argument in Sec. V.

4. Tracer particles

We monitor the diffusion of tracer particles [58,59] due to the local relaxations. We consider one tracer particle in each site of the elastoplastic model; each tracer particle moves randomly to one of the four nearest neighbors (in $d = 2$) after a plastic event in that site. The trajectory of the kth tracer particle is specified by $[x_k(t), y_k(t)]$. Typical trajectories of the tracer particles are shown in Fig. 15(a) as a function of time. In a timescale comparable to τ_α, the tracer travels over multiple sites in a very short time and spends most of the time without any activity. We then define the mean-squared displacement $\Delta^2(t)$ of the tracers by

$$\Delta^2(t) = \frac{1}{N_t}\sum_{k=1}^{N_t}\langle \Delta r_k^2(t)\rangle_{\text{time}}, \tag{B8}$$

where $\Delta r_k^2(t) = [x_k(t) - x_k(0)]^2 + [y_k(t) - y_k(0)]^2$ and N_t is the number of tracer particles. In Fig. 15(b), we show $\Delta^2(t)$ for different temperatures. We find a diffusive behavior at a larger time, $\Delta^2(t) = Dt$, from which we extract the diffusion coefficient D for each temperature.

APPENDIX C: AVALANCHES AT $T = 0^+$

1. Extremal dynamics

We explain the extremal dynamics at $T = 0^+$. In the finite-temperature simulations described in Appendix A, we take into account local thermal activation for a plastic event based on the probability $e^{-E(x)/T}$, where $E(x) = x^{3/2}$ at $0 \le x \le 1$. At vanishing temperature $T = 0^+$, this probability is extremely small. Therefore, the site with the smallest x, denoted as $x_{\min}$, associated with the lowest energy barrier $E_{\min} = x_{\min}^{3/2}$, shows the next plastic event. Thus, in practice, one can choose the weakest site having $x_{\min}$ sequentially instead of asking $e^{-E(x)/T}$ each time and waiting until it shows an event. This algorithm enormously accelerates dynamics and allows us to access information about plastic activities even at $T = 0^+$. This is the so-called *extremal dynamics* [48,80,81].

Finding one $x_{\min}$ corresponds to one simulation step. This is not directly related to physical time (that is why one can simulate it even at $T = 0^+$), yet one can associate the simulation step with the size of an avalanche (see below). Simulations start with the same initial condition used in the finite-temperature simulations. The system enters the stationary state after passing the initial transient regime. We carefully check the stationarity by monitoring the waiting time dependence of $P(x)$. We report data taken only from the stationary state.

In Fig. 16, we show a representative trajectory of $x_{\min}$ during an extremal dynamics simulation at the stationary state, which is an analog of Fig. 5 in Ref. [80] for a model for self-organized criticality. Typically, the weakest site with $x_{\min}(s)$ at a simulation step s induces the next weakest site at step $s+1$ with $x_{\min}(s+1)$ at a neighbor region because of elastic interactions. In particular, $x_{\min}(s) > x_{\min}(s+1)$, when the previous weakest site at step s destabilizes the next weakest site at step $s+1$. Therefore, a sequence of the weakest sites is dynamically correlated, forming an avalanche until the last weakest site is found at an uncorrelated place with a higher value of $x_{\min}$. The determination of uncorrelation and, hence, the termination of an avalanche has some ambiguity. Thus, following previous works, we introduce the threshold x_0 below which a sequence of $x_{\min}$ is correlated. In particular, we define the size of *event-based* avalanche, S, by the number

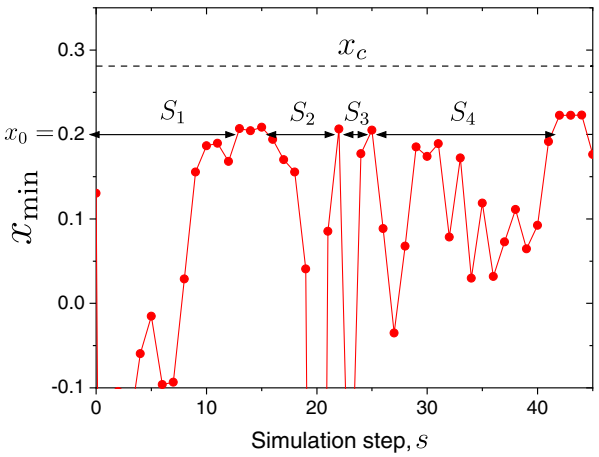

FIG. 16. An example of the evolution of $x_{\min}$ during the extremal dynamics at a steady state for the scalar model. The system size is $L = 256$. A series of event-based avalanche sizes, $S_1, S_2, \ldots$, are presented based on the threshold value $x_0 = 0.2$. $x_c = 0.281$ is indicated by the horizontal dashed line.

of chosen $x_{\min}$ forming a sequence with $x_{\min} < x_0$ (in other words, the duration of simulation steps with $x_{\min} < x_0$). As shown in Fig. 16, one can extract a series of event-based avalanche sizes, $S_1, S_2, \ldots$, from the trajectory of the extremal dynamics simulation. A given site may be chosen as the weakest site several times during one avalanche formation, which all contribute to S. Instead, one can define the size of *site-based* avalanche, $\tilde{S}$, by the number of sites participating in a single avalanche. By construction, $\tilde{S} \leq S$. The distinction between S and $\tilde{S}$ provides us with important physical information about the accumulation of multiple relaxation activities, which leads to an argument about the Stokes-Einstein violation, as discussed in Sec. V.

By construction, S and $\tilde{S}$ depend on the threshold value x_0. As x_0 is increased, the size of avalanches, S and $\tilde{S}$, increases. As we discuss further below, avalanches become system spanning when $x_0 \to x_c$, where x_c is the critical value associated with the critical energy gap $E_c = x_c^{3/2}$. We vary x_0 systematically to probe the critical behavior associated with x_c (see below).

2. Avalanche statistics

We describe how to analyze the avalanche data obtained during $T = 0^+$ extremal dynamics simulations. During simulations, we record the series of the event- and site-based avalanche sizes, given by $\{S_1, S_2, \ldots, S_M\}$ and $\{\tilde{S}_1, \tilde{S}_2, \ldots, \tilde{S}_M\}$, respectively, where M is the number of data points. In this paper, we analyze S and $\tilde{S}$ in parallel. Below, we explain how to analyze the data using S, but the same procedures are applied for $\tilde{S}$. We first define the mth moments of avalanche distribution ($m = 1, 2, \ldots$) by

$$\langle S^m \rangle = \int_0^\infty dS P(S) S^m = \frac{1}{M} \sum_{k=1}^{M} S_k^m, \tag{C1}$$

where $P(S)$ is the distribution of avalanches. One expects that $P(S)$ follows a power-law distribution:

$$P(S) \sim S^{-\tau} g(S/S_c), \tag{C2}$$

where τ is a critical exponent, S_c is a cutoff size, and $g(z)$ is a scaling function. Figure 17 shows $P(S)$ and $P(\tilde{S})$ for several x_0 for the scalar model. These plots demonstrate that the size of avalanches (both S and $\tilde{S}$) grows with increasing x_0, as expected. In particular, a scale-free, power-law behavior (with the eventual cutoff) is being developed by approaching the critical point x_c, which proves that x_0 is the relevant parameter that dictates the critical behavior of the system.

Assuming Eq. (C2) and $1 < \tau < 2$, one obtains

$$\langle S^m \rangle \sim \int_0^\infty dS S^{m-\tau} g(S/S_c) \sim S_c^{m+1-\tau}, \tag{C3}$$

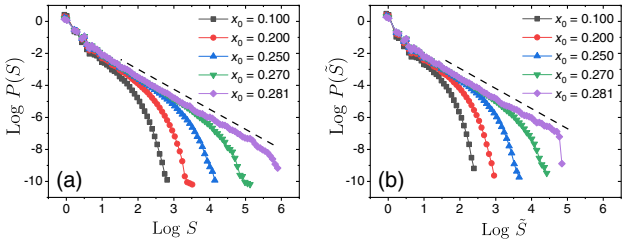

FIG. 17. Avalanche distributions $P(S)$ (a) and $P(\tilde{S})$ (b) for several x_0 approaching the critical point $x_c = x_0 = 0.281$ for the scalar model with $L = 256$. The dashed lines in (a) and (b) follow $P(S) \sim S^{-\tau}$ and $P(\tilde{S}) \sim S^{-\tilde{\tau}}$, respectively.

which implies $S_c \sim \langle S^{m+1} \rangle / \langle S^m \rangle$. Thus, in practice, we *define* S_c by $S_c = \langle S^3 \rangle / \langle S^2 \rangle$. Following Ref. [83], we assume

$$S_c \sim (x_c - x_0)^{-1/\sigma} f\left(\frac{L^{d_f}}{(x_c - x_0)^{-1/\sigma}} \right), \tag{C4}$$

where $f(z) = 1$ for $z \gg 1$ and $f(z) = z$ for $z \to 0$. Thus, $S_c \sim L^{d_f}$ when $x_0 \to x_c$ and $S_c \sim (x_c - x_0)^{-1/\sigma}$ when $L \to \infty$. Figures 18(a) and 18(b) show S_c and $\tilde{S}_c$ approaching $x_0 \to x_c$ for the scalar model. Both S_c and $\tilde{S}_c$ increase with increasing x_0 with an eventual saturation due to a finite-size effect. One can see the expected behavior, $S_c \sim (x_c - x_0)^{-1/\sigma}$ at larger L ($\tilde{S}_c$ as well). We then perform the scaling collapse in Figs. 18(c) and 18(d) following the scaling form in Eq. (C4). These scaling plots determine the critical point $x_c = 0.281$ and the critical exponents $1/\sigma$,

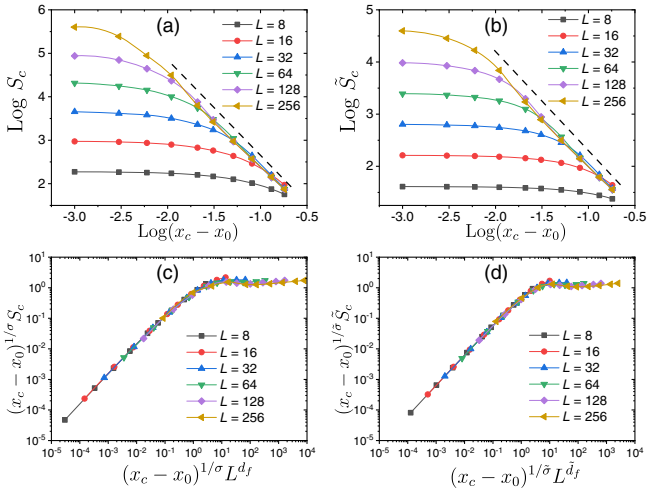

FIG. 18. Cutoff in avalanche distributions for the scalar model. (a),(b) $S_c = \langle S^3 \rangle / \langle S^2 \rangle$ (a) and $\tilde{S}_c = \langle \tilde{S}^3 \rangle / \langle \tilde{S}^2 \rangle$ (b) versus $x_c - x_0$ for various system sizes. The dashed lines in (a) and (b) follow $S_c \sim (x_c - x_0)^{-1/\sigma}$ and $\tilde{S}_c \sim (x_c - x_0)^{-1/\tilde{\sigma}}$, respectively. (c),(d) Scaling collapse assuming Eq. (C4). The critical point x_c and exponents σ, $\tilde{\sigma}$, d_f, and $\tilde{d}_f$ are determined by these scaling plots.

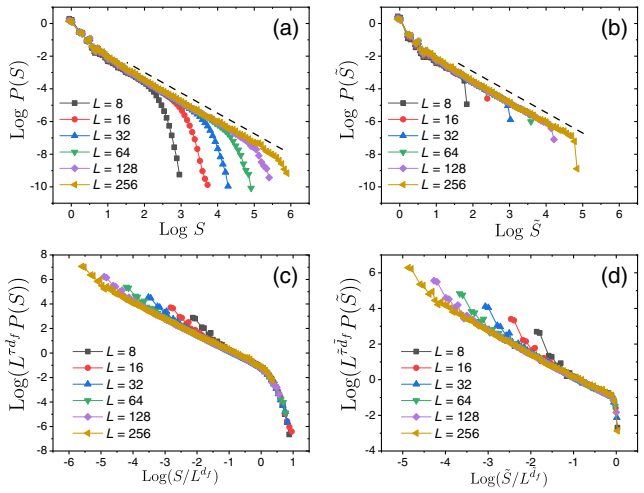

FIG. 19. (a),(b) Distribution of avalanche size $P(S)$ (a) and $P(\tilde{S})$ (b) for a stability threshold $x_0 = x_c$ for the scalar model, with varying the system size L. The dashed lines follow $P(S) \sim S^{-\tau}$ (a) and $P(\tilde{S}) \sim \tilde{S}^{-\tilde{\tau}}$ (b). (c) The corresponding scaling collapse following Eq. (C2) with $S_c \sim L^{d_f}$. (d) The same for $P(\tilde{S})$.

$1/\tilde{\sigma}$, d_f, and $\tilde{d}_f$ for the scalar model. The obtained values are reported in Table II.

Once the critical threshold x_c is determined, we measure avalanche distributions $P(S)$ and $P(\tilde{S})$ at $x_0 = x_c$, as shown in Figs. 19(a) and 19(b) for the scalar model. They show characteristic power-law behavior with cutoff S_c and $\tilde{S}_c$ due to a finite-size effect, which scales as $S_c \sim L^{d_f}$ and $\tilde{S}_c \sim L^{\tilde{d}_f}$, respectively. The power-law behavior determines τ and $\tilde{\tau}$, whose values are reported in Table II. We then perform scaling collapses in Figs. 19(c) and 19(d), following Eq. (C2), which validates the scaling ansatz and measured critical exponents.

Finally, we compute the distribution $P(x)$ from the configuration right before (or after) each avalanche defined by $x_0 = x_c$ starts (or ends). Thus, we exclude configurations during each avalanche and focus only on stable configurations expected to hold at strictly $T = 0$, where dynamics is not allowed. In Fig. 20(a), we show the measured $P(x)$ for the scalar model together with $P(x)$ obtained from the finite-temperature simulations. As T is lowered, $P(x)$ for finite T converges to $P(x)$ obtained from the extremal dynamics, whose functional form is consistent with $P(x) \sim (x - x_c)^{\theta}$, expected from other disordered systems. We then measure $\langle E_{\text{second}} - E_{\text{min}} \rangle \sim N^{-\delta}$ in Fig. 20(b), which encodes an important feature of the distribution of activation energy barriers at $T = 0$ (see Sec. IV for detail discussions). The obtained exponent δ is reported in Table II.

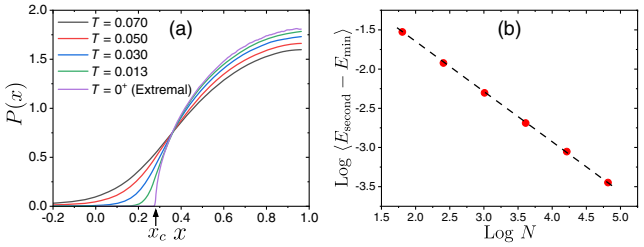

FIG. 20. (a) Distribution $P(x)$ for the scalar model with $L = 256$, obtained from the finite-temperature simulations and the extremal dynamics. The vertical arrow locates the critical threshold x_c. (b) $\langle E_{\text{second}} - E_{\text{min}} \rangle$, where the average is taken over configurations right before (or after) each avalanche formation, i.e., for which $x_{\text{min}} > x_0 = x_c$. The dashed line follows $\langle E_{\text{second}} - E_{\text{min}} \rangle \sim N^{-\delta}$.

[1] D. L. Anderson, *Through the Glass Lightly*, Science **267**, 1618 (1995).

[2] Mark D. Ediger, C. Austen Angell, and Sidney R. Nagel, *Supercooled Liquids and Glasses*, J. Phys. Chem. **100**, 13200 (1996).

[3] P. G. Debenedetti and F. H. Stillinger, *Supercooled Liquids and the Glass Transition*, Nature (London) **410**, 259 (2001).

[4] Ludovic Berthier and Giulio Biroli, *Theoretical Perspective on the Glass Transition and Amorphous Materials*, Rev. Mod. Phys. **83**, 587 (2011).

[5] Walter Kob, Claudio Donati, Steven J. Plimpton, Peter H. Poole, and Sharon C. Glotzer, *Dynamical Heterogeneities in a Supercooled Lennard-Jones Liquid*, Phys. Rev. Lett. **79**, 2827 (1997).

[6] Ryoichi Yamamoto and Akira Onuki, *Dynamics of Highly Supercooled Liquids: Heterogeneity, Rheology, and Diffusion*, Phys. Rev. E **58**, 3515 (1998).

[7] C. Dalle-Ferrier, C. Thibierge, C. Alba-Simionesco, L. Berthier, G. Biroli, J.-P. Bouchaud, F. Ladieu, D. L'Hôte, and G. Tarjus, *Spatial Correlations in the Dynamics of Glass-Forming Liquids: Experimental Determination of Their Temperature Dependence*, Phys. Rev. E **76**, 041510 (2007).

[8] Smarajit Karmakar, Chandan Dasgupta, and Srikanth Sastry, *Growing Length Scales and Their Relation to Timescales in Glass-Forming Liquids*, Annu. Rev. Condens. Matter Phys. **5**, 255 (2014).

[9] M. M. Hurley and Peter Harrowell, *Kinetic Structure of a Two-Dimensional Liquid*, Phys. Rev. E **52**, 1694 (1995).

[10] Theodore R. Kirkpatrick, Devarajan Thirumalai, and Peter G. Wolynes, *Scaling Concepts for the Dynamics of Viscous Liquids near an Ideal Glassy State*, Phys. Rev. A **40**, 1045 (1989).

[11] Vassiliy Lubchenko and Peter G. Wolynes, *Theory of Structural Glasses and Supercooled Liquids*, Annu. Rev. Phys. Chem. **58**, 235 (2007).

[12] G. Biroli and J.-P. Bouchaud, *The Random First-Order Transition Theory of Glasses: A Critical Assessment*, in *Structural Glasses and Supercooled Liquids: Theory, Experiment, and Applications* (Wiley, New York, 2012), pp. 31–113.

[13] Felix Ritort and Peter Sollich, *Glassy Dynamics of Kinetically Constrained Models*, Adv. Phys. **52**, 219 (2003).

[14] Ludovic Berthier, Giulio Biroli, Jean-Philippe Bouchaud, Luca Cipelletti, and Wim van Saarloos, *Dynamical Heterogeneities in Glasses, Colloids, and Granular Media* (Oxford, New York, 2011), Vol. 150.

[15] Juan P. Garrahan and David Chandler, *Geometrical Explanation and Scaling of Dynamical Heterogeneities in Glass Forming Systems*, Phys. Rev. Lett. **89**, 035704 (2002).

[16] Juan P. Garrahan, Robert L. Jack, Vivien Lecomte, Estelle Pitard, Kristina van Duijvendijk, and Frédéric van Wijland, *Dynamical First-Order Phase Transition in Kinetically Constrained Models of Glasses*, Phys. Rev. Lett. **98**, 195702 (2007).

[17] L. O. Hedges, R. L. Jack, J. P. Garrahan, and D. Chandler, *Dynamic Order-Disorder in Atomistic Models of Structural Glass Formers*, Science **323**, 1309 (2009).

[18] David Turnbull and Morrel H. Cohen, *Free-Volume Model of the Amorphous Phase: Glass Transition*, J. Chem. Phys. **34**, 120 (1961).

[19] J. C. Dyre, *Colloquium: The Glass Transition and Elastic Models of Glass-Forming Liquids*, Rev. Mod. Phys. **78**, 953 (2006).

[20] Corrado Rainone, Eran Bouchbinder, and Edan Lerner, *Pinching a Glass Reveals Key Properties of Its Soft Spots*, Proc. Natl. Acad. Sci. U.S.A. **117**, 5228 (2020).

[21] Geert Kapteijns, David Richard, Eran Bouchbinder, Thomas B. Schrøder, Jeppe C. Dyre, and Edan Lerner, *Does Mesoscopic Elasticity Control Viscous Slowing Down in Glass-Forming Liquids?*, J. Chem. Phys. **155**, 74502 (2021).

[22] Massimo Pica Ciamarra, Wencheng Ji, and Matthieu Wyart, *The Energy Cost of Local Rearrangements, Not Cooperative Effects, Makes Glasses Solid*, arXiv:2302.05150.

[23] Thomas B. Schrøder and Jeppe C. Dyre, *Solid-like Mean-Square Displacement in Glass-Forming Liquids*, J. Chem. Phys. **152**, 141101 (2020).

[24] A. Lemaître, *Structural Relaxation Is a Scale-Free Process*, Phys. Rev. Lett. **113**, 245702 (2014).

[25] Sadrul Chowdhury, Sneha Abraham, Toby Hudson, and Peter Harrowell, *Long Range Stress Correlations in the Inherent Structures of Liquids at Rest*, J. Chem. Phys. **144**, 124508 (2016).

[26] Hua Tong, Shiladitya Sengupta, and Hajime Tanaka, *Emergent Solidity of Amorphous Materials as a Consequence of Mechanical Self-Organisation*, Nat. Commun. **11**, 1 (2020).

[27] Bin Wu, Takuya Iwashita, and Takeshi Egami, *Anisotropic Stress Correlations in Two-Dimensional Liquids*, Phys. Rev. E **91**, 032301 (2015).

[28] Manuel Maier, Annette Zippelius, and Matthias Fuchs, *Emergence of Long-Ranged Stress Correlations at the Liquid to Glass Transition*, Phys. Rev. Lett. **119**, 265701 (2017).

[29] David Steffen, Ludwig Schneider, Marcus Müller, and Jörg Rottler, *Molecular Simulations and Hydrodynamic Theory of Nonlocal Shear-Stress Correlations in Supercooled Fluids*, J. Chem. Phys. **157**, 064501 (2022).

[30] Elijah Flenner and Grzegorz Szamel, *Long-Range Spatial Correlations of Particle Displacements and the Emergence of Elasticity*, Phys. Rev. Lett. **114**, 025501 (2015).

[31] L. Klochko, J. Baschnagel, J. P. Wittmer, H. Meyer, O. Benzerara, and A. N. Semenov, *Theory of Length-Scale Dependent Relaxation Moduli and Stress Fluctuations in Glass-Forming and Viscoelastic Liquids*, J. Chem. Phys. **156**, 164505 (2022).

[32] Rahul N. Chacko, François P. Landes, Giulio Biroli, Olivier Dauchot, Andrea J. Liu, and David R. Reichman, *Elastoplasticity Mediates Dynamical Heterogeneity below the Mode Coupling Temperature*, Phys. Rev. Lett. **127**, 048002 (2021).

[33] Matthias Lerbinger, Armand Barbot, Damien Vandembroucq, and Sylvain Patinet, *Relevance of Shear Transformations in the Relaxation of Supercooled Liquids*, Phys. Rev. Lett. **129**, 195501 (2022).

[34] Michael L. Falk and James S. Langer, *Dynamics of Viscoplastic Deformation in Amorphous Solids*, Phys. Rev. E **57**, 7192 (1998).

[35] Misaki Ozawa and Giulio Biroli, *Elasticity, Facilitation, and Dynamic Heterogeneity in Glass-Forming Liquids*, Phys. Rev. Lett. **130**, 138201 (2023).

[36] Guillemette Picard, Armand Ajdari, François Lequeux, and Lydéric Bocquet, *Elastic Consequences of a Single Plastic Event: A Step towards the Microscopic Modeling of the Flow of Yield Stress Fluids*, Eur. Phys. J. E **15**, 371 (2004).

[37] A. Nicolas, E. E. Ferrero, K. Martens, and J.-L. Barrat, *Deformation and Flow of Amorphous Solids: Insights from Elastoplastic Models*, Rev. Mod. Phys. **90**, 045006 (2018).

[38] D. Vandembroucq, R. Skoe, and S. Roux, *Universal Depinning Force Fluctuations of an Elastic Line: Application to Finite Temperature Behavior*, Phys. Rev. E **70**, 051101 (2004).

[39] J. Lin, E. Lerner, A. Rosso, and M. Wyart, *Scaling Description of the Yielding Transition in Soft Amorphous Solids at Zero Temperature*, Proc. Natl. Acad. Sci. U.S.A. **111**, 14382 (2014).

[40] Saverio Rossi, Giulio Biroli, Misaki Ozawa, Gilles Tarjus, and Francesco Zamponi, *Finite-Disorder Critical Point in the Yielding Transition of Elastoplastic Models*, Phys. Rev. Lett. **129**, 228002 (2022).

[41] Ludovic Berthier, Giulio Biroli, J.-P. Bouchaud, Luca Cipelletti, D. El Masri, Denis L'Hôte, Francois Ladieu, and Matteo Pierno, *Direct Experimental Evidence of a Growing Length Scale Accompanying the Glass Transition*, Science **310**, 1797 (2005).

[42] M. Popović, T. W. J. de Geus, W. Ji, and M. Wyart, *Thermally Activated Flow in Models of Amorphous Solids*, Phys. Rev. E **104**, 025010 (2021).

[43] Raphaël Candelier, Asaph Widmer-Cooper, Jonathan K. Kummerfeld, Olivier Dauchot, Giulio Biroli, Peter Harrowell, and David R. Reichman, *Spatiotemporal Hierarchy of Relaxation Events, Dynamical Heterogeneities, and Structural Reorganization in a Supercooled Liquid*, Phys. Rev. Lett. **105**, 135702 (2010).

[44] Aaron S. Keys, Lester O. Hedges, Juan P. Garrahan, Sharon C. Glotzer, and David Chandler, *Excitations Are Localized and Relaxation Is Hierarchical in Glass-Forming Liquids*, Phys. Rev. X **1**, 021013 (2011).

[45] Taiki Yanagishima, John Russo, and Hajime Tanaka, *Common Mechanism of Thermodynamic and Mechanical Origin for Ageing and Crystallization of Glasses*, Nat. Commun. **8**, 1 (2017).
[46] James P. Sethna, Karin A. Dahmen, and Christopher R. Myers, *Crackling Noise*, Nature (London) **410**, 242 (2001).
[47] Alberto Rosso, James P. Sethna, and Matthieu Wyart, *Avalanches and Deformation in Glasses and Disordered Systems*, arXiv:2208.04090.
[48] Víctor Hugo Purrello, Jose Luis Iguain, Alejandro Benedykt Kolton, and Eduardo Alberto Jagla, *Creep and Thermal Rounding close to the Elastic Depinning Threshold*, Phys. Rev. E **96**, 022112 (2017).
[49] Liheng Yao and Robert L. Jack, *Thermal Vestiges of Avalanches in the Driven Random Field Ising Model*, J. Stat. Mech. (2023) 023303.
[50] Daniel Korchinski and Jörg Rottler, *Dynamic Phase Diagram of Plastically Deformed Amorphous Solids at Finite Temperature*, Phys. Rev. E **106**, 034103 (2022).
[51] Benjamin Guiselin, Camille Scalliet, and Ludovic Berthier, *Microscopic Origin of Excess Wings in Relaxation Spectra of Supercooled Liquids*, Nat. Phys. **18**, 468 (2022).
[52] Camille Scalliet, Benjamin Guiselin, and Ludovic Berthier, *Thirty Milliseconds in the Life of a Supercooled Liquid*, Phys. Rev. X **12**, 041028 (2022).
[53] Gilles Tarjus and Daniel Kivelson, *Breakdown of the Stokes-Einstein Relation in Supercooled Liquids*, J. Chem. Phys. **103**, 3071 (1995).
[54] Mark D. Ediger, *Spatially Heterogeneous Dynamics in Supercooled Liquids*, Annu. Rev. Phys. Chem. **51**, 99 (2000).
[55] Shiladitya Sengupta, Smarajit Karmakar, Chandan Dasgupta, and Srikanth Sastry, *Breakdown of the Stokes-Einstein Relation in Two, Three, and Four Dimensions*, J. Chem. Phys. **138**, 12A548 (2013).
[56] Patrick Charbonneau, Yuliang Jin, Giorgio Parisi, and Francesco Zamponi, *Hopping and the Stokes-Einstein Relation Breakdown in Simple Glass Formers*, Proc. Natl. Acad. Sci. U.S.A. **111**, 15025 (2014).
[57] Takeshi Kawasaki and Kang Kim, *Identifying Time Scales for Violation/Preservation of Stokes-Einstein Relation in Supercooled Water*, Sci. Adv. **3**, e1700399 (2017).
[58] YounJoon Jung, Juan P. Garrahan, and David Chandler, *Excitation Lines and the Breakdown of Stokes-Einstein Relations in Supercooled Liquids*, Phys. Rev. E **69**, 061205 (2004).
[59] Ludovic Berthier, David Chandler, and Juan P. Garrahan, *Length Scale for the Onset of Fickian Diffusion in Supercooled Liquids*, Europhys. Lett. **69**, 320 (2004).
[60] Lester O. Hedges, Lutz Maibaum, David Chandler, and Juan P. Garrahan, *Decoupling of Exchange and Persistence Times in Atomistic Models of Glass Formers*, J. Chem. Phys. **127**, 211101 (2007).
[61] Pinaki Chaudhuri, Ludovic Berthier, and Walter Kob, *Universal Nature of Particle Displacements close to Glass and Jamming Transitions*, Phys. Rev. Lett. **99**, 060604 (2007).
[62] Raffaele Pastore, Takuma Kikutsuji, Francesco Rusciano, Nobuyuki Matubayasi, Kang Kim, and Francesco Greco, *Breakdown of the Stokes-Einstein Relation in Supercooled Liquids: A Cage-Jump Perspective*, J. Chem. Phys. **155**, 114503 (2021).
[63] V. V. Bulatov and A. S. Argon, *A Stochastic Model for Continuum Elasto-plastic Behavior. II. A Study of the Glass Transition and Structural Relaxation*, Model. Simul. Mater. Sci. Eng. **2**, 185 (1994).
[64] Ezequiel E. Ferrero, Kirsten Martens, and Jean-Louis Barrat, *Relaxation in Yield Stress Systems through Elastically Interacting Activated Events*, Phys. Rev. Lett. **113**, 248301 (2014).
[65] Eduardo Alberto Jagla, *Tensorial Description of the Plasticity of Amorphous Composites*, Phys. Rev. E **101**, 043004 (2020).
[66] Ezequiel E. Ferrero, Alejandro B. Kolton, and Eduardo A. Jagla, *Yielding of Amorphous Solids at Finite Temperatures*, Phys. Rev. Mater. **5**, 115602 (2021).
[67] Gieberth Rodriguez-Lopez, Kirsten Martens, and Ezequiel E. Ferrero, *Temperature Dependence of Fast Relaxation Processes in Amorphous Materials*, arXiv:2302.06471.
[68] Yue Fan, Takuya Iwashita, and Takeshi Egami, *How Thermally Activated Deformation Starts in Metallic Glass*, Nat. Commun. **5**, 5083 (2014).
[69] I. Fernández Aguirre and Eduardo Alberto Jagla, *Critical Exponents of the Yielding Transition of Amorphous Solids*, Phys. Rev. E **98**, 013002 (2018).
[70] Craig E. Maloney and Anael Lemaitre, *Amorphous Systems in Athermal, Quasistatic Shear*, Phys. Rev. E **74**, 016118 (2006).
[71] Full isotropy is slightly broken by the choice of biperiodic boundary conditions.
[72] Claudio Donati, Silvio Franz, Sharon C. Glotzer, and Giorgio Parisi, *Theory of Non-linear Susceptibility and Correlation Length in Glasses and Liquids*, J. Non-Cryst. Solids **307**, 215 (2002).
[73] Simone Capaccioli, Giancarlo Ruocco, and Francesco Zamponi, *Dynamically Correlated Regions and Configurational Entropy in Supercooled Liquids*, J. Phys. Chem. B **112**, 10652 (2008).
[74] Olivier Dauchot, François Ladieu, and C. Patrick Royall, *The Glass Transition in Molecules, Colloids and Grains: Universality and Specificity*, arXiv:2211.03158.
[75] Smarajit Karmakar, Chandan Dasgupta, and Srikanth Sastry, *Growing Length and Time Scales in Glass-Forming Liquids*, Proc. Natl. Acad. Sci. U.S.A. **106**, 3675 (2009).
[76] Daniele Coslovich, Misaki Ozawa, and Walter Kob, *Dynamic and Thermodynamic Crossover Scenarios in the Kob-Andersen Mixture: Insights from Multi-CPU and Multi-GPU Simulations*, Eur. Phys. J. E **41**, 1 (2018).
[77] Saurish Chakrabarty, Indrajit Tah, Smarajit Karmakar, and Chandan Dasgupta, *Block Analysis for the Calculation of Dynamic and Static Length Scales in Glass-Forming Liquids*, Phys. Rev. Lett. **119**, 205502 (2017).
[78] N. Lačević, Francis W. Starr, T. B. Schrøder, and Sharon C. Glotzer, *Spatially Heterogeneous Dynamics Investigated via a Time-Dependent Four-Point Density Correlation Function*, J. Chem. Phys. **119**, 7372 (2003).
[79] We are considering either finite systems or the thermodynamic limit taken after the zero-temperature limit.

[80] Maya Paczuski, Sergei Maslov, and Per Bak, *Avalanche Dynamics in Evolution, Growth, and Depinning Models*, Phys. Rev. E **53**, 414 (1996).
[81] J.-C. Baret, D. Vandembroucq, and S. Roux, *Extremal Model for Amorphous Media Plasticity*, Phys. Rev. Lett. **89**, 195506 (2002).
[82] Dheeraj Kumar, Sylvain Patinet, Craig E. Maloney, Ido Regev, Damien Vandembroucq, and Muhittin Mungan, *Mapping out the Glassy Landscape of a Mesoscopic Elastoplastic Model*, J. Chem. Phys. **157**, 174504 (2022).
[83] Jihui Han, Wei Li, and Weibing Deng, *Critical Behavior of a Generalized Bak-Sneppen Model*, J. Phys. Conf. Ser. **1113**, 012011 (2018).
[84] J. Lin, A. Saade, E. Lerner, A. Rosso, and M. Wyart, *On the Density of Shear Transformations in Amorphous Solids*, Europhys. Lett. **105**, 26003 (2014).
[85] S. Karmakar, E. Lerner, and I. Procaccia, *Statistical Physics of the Yielding Transition in Amorphous Solids*, Phys. Rev. E **82**, 055103(R) (2010).
[86] Markus Müller and Matthieu Wyart, *Marginal Stability in Structural, Spin, and Electron Glasses*, Annu. Rev. Condens. Matter Phys. **6**, 177 (2015).
[87] A. Lemaître and C. Caroli, *Plastic Response of a 2D Amorphous Solid to Quasi-Static Shear: II—Dynamical Noise and Avalanches in a Mean Field Model*, arXiv. 0705.3122.
[88] Jie Lin and Matthieu Wyart, *Mean-Field Description of Plastic Flow in Amorphous Solids*, Phys. Rev. X **6**, 011005 (2016).
[89] Ezequiel E. Ferrero and Eduardo A. Jagla, *Properties of the Density of Shear Transformations in Driven Amorphous Solids*, J. Phys. Condens. Matter **33**, 124001 (2021).
[90] Daniel Korchinski, Céline Ruscher, and Jörg Rottler, *Signatures of the Spatial Extent of Plastic Events in the Yielding Transition in Amorphous Solids*, Phys. Rev. E **104**, 034603 (2021).
[91] Massimo Pica Ciamarra, Raffaele Pastore, and Antonio Coniglio, *Particle Jumps in Structural Glasses*, Soft Matter **12**, 358 (2016).
[92] Stephen F. Swallen, Paul A. Bonvallet, Robert J. McMahon, and M. D. Ediger, *Self-Diffusion of Tris-Naphthylbenzene near the Glass Transition Temperature*, Phys. Rev. Lett. **90**, 015901 (2003).
[93] Francesco Mallamace, Caterina Branca, Carmelo Corsaro, Nancy Leone, Jeroen Spooren, Sow-Hsin Chen, and H. Eugene Stanley, *Transport Properties of Glass-Forming Liquids Suggest That Dynamic Crossover Temperature Is As Important As the Glass Transition Temperature*, Proc. Natl. Acad. Sci. U.S.A. **107**, 22457 (2010).
[94] In fact, in some kinetically constrained models [95], the fractional Stokes-Einstein violation (with a similar value of ζ with experiments) was conjectured based on numerical data and physical arguments. Recent rigorous results [96] showed that this is not what happens, but there is likely a violation as the one we find. This suggests that the logarithmic Stokes-Einstein violation can be easily misinterpreted as a fractional one with a small exponent $1-\zeta$.
[95] Juan P. Garrahan, Peter Sollich, and Cristina Toninelli, *Kinetically Constrained Models*, in *Dynamical Heterogeneities in Glasses, Colloids, and Granular Media* (Oxford, New York, 2011), pp. 111–137.
[96] Oriane Blondel and Cristina Toninelli, *Is There a Fractional Breakdown of the Stokes-Einstein Relation in Kinetically Constrained Models at Low Temperature?*, Europhys. Lett. **107**, 26005 (2014).
[97] Misaki Ozawa, Kang Kim, and Kunimasa Miyazaki, *Tuning Pairwise Potential Can Control the Fragility of Glass-Forming Liquids: From a Tetrahedral Network to Isotropic Soft Sphere Models*, J. Stat. Mech. (2016) 074002.
[98] Sivert H. Glarum, *Dielectric Relaxation of Isoamyl Bromide*, J. Chem. Phys. **33**, 639 (1960).
[99] Muhammad R. Hasyim and Kranthi K. Mandadapu, *A Theory of Localized Excitations in Supercooled Liquids*, J. Chem. Phys. **155**, 044504 (2021).
[100] Christian Rehwald, Oliver Rubner, and Andreas Heuer, *From Coupled Elementary Units to the Complexity of the Glass Transition*, Phys. Rev. Lett. **105**, 117801 (2010).
[101] Christian Rehwald and Andreas Heuer, *How Coupled Elementary Units Determine the Dynamics of Macroscopic Glass-Forming Systems*, Phys. Rev. E **86**, 051504 (2012).
[102] Camille Scalliet, Benjamin Guiselin, and Ludovic Berthier, *Excess Wings and Asymmetric Relaxation Spectra in a Facilitated Trap Model*, J. Chem. Phys. **155**, 064505 (2021).
[103] Masaharu Isobe, Aaron S. Keys, David Chandler, and Juan P. Garrahan, *Applicability of Dynamic Facilitation Theory to Binary Hard Disk Systems*, Phys. Rev. Lett. **117**, 145701 (2016).
[104] Yael S. Elmatad, Robert L. Jack, David Chandler, and Juan P. Garrahan, *Finite-Temperature Critical Point of a Glass Transition*, Proc. Natl. Acad. Sci. U.S.A. **107**, 12793 (2010).
[105] Francesco Turci, C. Patrick Royall, and Thomas Speck, *Nonequilibrium Phase Transition in an Atomistic Glass Former: The Connection to Thermodynamics*, Phys. Rev. X **7**, 031028 (2017).
[106] Elisabeth Agoritsas, Eric Bertin, Kirsten Martens, and Jean-Louis Barrat, *On the Relevance of Disorder in Athermal Amorphous Materials under Shear*, Eur. Phys. J. E **38**, 1 (2015).
[107] H. Tanaka, T. Kawasaki, H. Shintani, and K. Watanabe, *Critical-like Behaviour of Glass-Forming Liquids*, Nat. Mater. **9**, 324 (2010).
[108] C. Patrick Royall and Stephen R. Williams, *The Role of Local Structure in Dynamical Arrest*, Phys. Rep. **560**, 1 (2015).
[109] Hajime Tanaka, Hua Tong, Rui Shi, and John Russo, *Revealing Key Structural Features Hidden in Liquids and Glasses*, Nat. Rev. Phys. **1**, 333 (2019).
[110] Joris Paret, Robert L. Jack, and Daniele Coslovich, *Assessing the Structural Heterogeneity of Supercooled Liquids through Community Inference*, J. Chem. Phys. **152**, 144502 (2020).
[111] Asaph Widmer-Cooper, Peter Harrowell, and H. Fynewever, *How Reproducible Are Dynamic Heterogeneities in a Supercooled Liquid?*, Phys. Rev. Lett. **93**, 135701 (2004).

[112] A. Widmer-Cooper, H. Perry, P. Harrowell, and D. R. Reichman, *Irreversible Reorganization in a Supercooled Liquid Originates from Localized Soft Modes*, Nat. Phys. **4**, 711 (2008).

[113] Glen M. Hocky, Daniele Coslovich, Atsushi Ikeda, and David R. Reichman, *Correlation of Local Order with Particle Mobility in Supercooled Liquids Is Highly System Dependent*, Phys. Rev. Lett. **113**, 157801 (2014).

[114] Anaël Lemaître, Chandana Mondal, Michael Moshe, Itamar Procaccia, Saikat Roy, and Keren Screiber-Re'em, *Anomalous Elasticity and Plastic Screening in Amorphous Solids*, Phys. Rev. E **104**, 024904 (2021).

[115] E. Lerner, E. DeGiuli, G. Düring, and M. Wyart, *Breakdown of Continuum Elasticity in Amorphous Solids*, Soft Matter **10**, 5085 (2014).

[116] Chen Liu, Suman Dutta, Pinaki Chaudhuri, and Kirsten Martens, *Elastoplastic Approach Based on Microscopic Insights for the Steady State and Transient Dynamics of Sheared Disordered Solids*, Phys. Rev. Lett. **126**, 138005 (2021).

[117] David Fernández Castellanos, Stéphane Roux, and Sylvain Patinet, *Insights from the Quantitative Calibration of an Elasto-plastic Model from a Lennard-Jones Atomic Glass*, C. R. Phys. **22**, 1 (2021).

[118] David F. Castellanos, Stéphane Roux, and Sylvain Patinet, *History Dependent Plasticity of Glass: A Mapping between Atomistic and Elasto-plastic Models*, Acta Mater. **241**, 118405 (2022).

[119] Indrajit Tah, Sean A. Ridout, and Andrea J. Liu, *Fragility in Glassy Liquids: A Structural Approach Based on Machine Learning*, J. Chem. Phys. **157**, 124501 (2022).

[120] Hongyi Xiao, Ge Zhang, Entao Yang, Robert J. S. Ivancic, Sean A. Ridout, Robert Riggleman, Douglas J. Durian, and Andrea J. Liu, *Machine Learning-Informed Structuro-elastoplasticity Predicts Ductility of Disordered Solids*, arXiv:2303.12486.

[121] Tina Hecksher and Jeppe C. Dyre, *A Review of Experiments Testing the Shoving Model*, J. Non-Cryst. Solids **407**, 14 (2015).

[122] Wencheng Ji, Tom W. J. de Geus, Elisabeth Agoritsas, and Matthieu Wyart, *Mean-Field Description for the Architecture of Low-Energy Excitations in Glasses*, Phys. Rev. E **105**, 044601 (2022).

[123] Daniele Coslovich and Giorgio Pastore, *Understanding Fragility in Supercooled Lennard-Jones Mixtures. I. Locally Preferred Structures*, J. Chem. Phys. **127**, 124504 (2007).

[124] Giulio Biroli and Jean-Philippe Bouchaud, *The RFOT Theory of Glasses: Recent Progress and Open Issues*, arXiv:2208.05866.

[125] David Fernandez Castellanos and Michael Zaiser, *Avalanche Behavior in Creep Failure of Disordered Materials*, Phys. Rev. Lett. **121**, 125501 (2018).

[126] T. Bauer, J. Oberdisse, and L. Ramos, *Collective Rearrangement at the Onset of Flow of a Polycrystalline Hexagonal Columnar Phase*, Phys. Rev. Lett. **97**, 258303 (2006).

[127] F. Caton and C. Baravian, *Plastic Behavior of Some Yield Stress Fluids: From Creep to Long-Time Yield*, Rheol. Acta **47**, 601 (2008).

[128] T. Divoux, C. Barentin, and S. Manneville, *From Stress-Induced Fluidization Processes to Herschel-Bulkley Behaviour in Simple Yield Stress Fluids*, Soft Matter **7**, 8409 (2011).

[129] M. Siebenbürger, M. Ballauff, and T. Voigtmann, *Creep in Colloidal Glasses*, Phys. Rev. Lett. **108**, 255701 (2012).

[130] V. Grenard, T. Divoux, N. Taberlet, and S. Manneville, *Timescales in Creep and Yielding of Attractive Gels*, Soft Matter **10**, 1555 (2014).

[131] M. Leocmach, C. Perge, T. Divoux, and S. Manneville, *Creep and Fracture of a Protein Gel under Stress*, Phys. Rev. Lett. **113**, 038303 (2014).

[132] Sebastian Bustingorry, A. B. Kolton, and Thierry Giamarchi, *Thermal Rounding of the Depinning Transition*, Europhys. Lett. **81**, 26005 (2007).

[133] Alejandro B. Kolton, Alberto Rosso, and Thierry Giamarchi, *Creep Motion of an Elastic String in a Random Potential*, Phys. Rev. Lett. **94**, 047002 (2005).

[134] Ludovic Berthier and Walter Kob, *The Monte Carlo Dynamics of a Binary Lennard-Jones Glass-Forming Mixture*, J. Phys. Condens. Matter **19**, 205130 (2007).

[135] Craig E. Maloney and Daniel J. Lacks, *Energy Barrier Scalings in Driven Systems*, Phys. Rev. E **73**, 061106 (2006).

[136] Armand Barbot, Matthias Lerbinger, Anier Hernandez-Garcia, Reinaldo García-García, Michael L. Falk, Damien Vandembroucq, and Sylvain Patinet, *Local Yield Stress Statistics in Model Amorphous Solids*, Phys. Rev. E **97**, 033001 (2018).

[137] Marko Popović, Tom W. J. de Geus, and Matthieu Wyart, *Elastoplastic Description of Sudden Failure in Athermal Amorphous Materials during Quasistatic Loading*, Phys. Rev. E **98**, 040901(R) (2018).

[138] Joseph Pollard and Suzanne M. Fielding, *Yielding, Shear Banding, and Brittle Failure of Amorphous Materials*, Phys. Rev. Res. **4**, 043037 (2022).

[139] Elijah Flenner, Hannah Staley, and Grzegorz Szamel, *Universal Features of Dynamic Heterogeneity in Supercooled Liquids*, Phys. Rev. Lett. **112**, 097801 (2014).

[140] Kang Kim and Shinji Saito, *Multiple Length and Time Scales of Dynamic Heterogeneities in Model Glass-Forming Liquids: A Systematic Analysis of Multi-point and Multi-time Correlations*, J. Chem. Phys. **138**, 12A506 (2013).

[141] Giulio Biroli, Kunimasa Miyazaki, and David R. Reichman, *Dynamical Heterogeneity in Glass-Forming Liquids*, arXiv:2209.02825.

[142] Elijah Flenner and Grzegorz Szamel, *Dynamic Heterogeneity in Two-Dimensional Supercooled Liquids: Comparison of Bond-Breaking and Bond-Orientational Correlations*, J. Stat. Mech. (2016) 074008.